Measurement of Heavy Ion induced X-ray production cross sections in metallic targets at MeV energies

by

Masedi Carington Masekane

submitted in accordance with the requirements for

the degree of

Master of Science

in the subject

Physics

at the

University of South Africa

Supervisor: Dr. S.J. Moloi (University of South Africa)

Co-Supervisor: Prof. M. Msimanga (Tshwane University of Technology)

April 2019

Declaration

Name: Masedi Carington Masekane

Student number: 62700022

Degree: MSc. Physics

Measurement of Heavy Ion induced X-ray production cross sections in metallic targets at MeV energies

I declare that the above dissertation is my own work and that all the sources that I have used or quoted have been indicated and acknowledged by means of complete references.

I further declare that I submitted the dissertation to originality checking software and that it falls within the accepted requirements for originality.

I further declare that I have not previously submitted this work, or part of it, for examination at the University of South Africa for another qualification or at any other higher education institution.

20/04/2019

SIGNATURE DATE

Abstract

Experimental X-ray production cross sections (i.e. probability of X-ray generation in a target by an incoming MeV ion) are useful not only for fundamental ion beam – matter interaction studies, but also for the development of new ion beam materials analysis techniques such as Heavy Ion Particle Induced X-ray Emission (HI-PIXE) spectroscopy. Unfortunately, while theoretical predictions of X-ray production cross sections due to light ($Z<6$) projectile ions are generally in good agreement with experiment, this is not the same for heavier projectiles. Experimental studies show that heavy ions induce higher X-ray yields in targets compared to light ions of the same velocity, which implies higher sensitivity for Heavy Ion PIXE. There is therefore a need for substantial experimental data to improve theoretical models. This dissertation presents measurements carried out at the iThemba Laboratory for Accelerator Based Sciences (LABS) to determine X-ray production cross sections in Vanadium (V), Zirconium (Zr) and Tin (Sn) metal oxide films due to carbon and chlorine MeV ion beams at an ion velocity range of 0.1-1.0 MeV/u. The measured cross sections are compared to predictions by the modified Plane Wave Born Approximation (PWBA) and the ECPSSR theory that takes into account; the energy loss (E) of the projectile due to Coulomb deflection (C) by the target atom, and the perturbed-stationary state (PSS) and relativistic nature (R) of the target atoms' inner shell. The observed agreements and discrepancies between experiment and theory are discussed in terms of the atomic ionization mechanisms for each projectile-target collision.

Acknowledgements

Foremost I would like to acknowledge my parents who have inspired in me an inquisitive mind from which my quest for knowledge from a kinder age continues to enrich myself and others. To my Father, Nakampe Masekane, for your constant guidance, parental vigilance, being above absolute in fatherhood in all my study years. To my Mother, Dikeledi Masekane, for always believing in me and seeing the scientist in me from as early as Grade 11. I can never thank the both of you enough. All that I am has always been through your greatest of guidance and wisdom.

For the work presented in this dissertation, I would like to acknowledge Prof. Mandla Msimanga (TUT), for his consistent patience and will to teach, overall moral and academic support throughout my study years, for inspiring growth in my undergraduate study years and being a guardian always open to lend a hand; I humbly thank you. May God Bless you and your family for your good work. To Dr. Sabata J Moloi (UNISA), for making my MSc journey a rich, open, and fun filled journey. For always being willing to go the extra mile, I give my humble gratitude.

To Dr. Morgan Madhuku (iThemba LABS), for your grooming and expert advice in Ion Beam Analysis and PIXE analysis. To Prof. Carlos Pineda-Vargas, Dr. Phillip Sechogela, the Department of Physics of the College of Science, Engineering and Technology of the University of South Africa (UNISA), the Department of Physics of the Tshwane University of Technology, the iThemba Laboratory for Accelerator Based Sciences (LABS), the International Atomic Energy Agency (IAEA) [CRP F11019], the National Research Foundation (NRF) [105292], the Department of Science and Technology (DST), the Department of Higher Education and Training and the Government of the Republic of South Africa; for their vital roles in enabling the successful

progression and completion of the academic and scientific project reported herein through infrastructural, material and financial support, I express my humble gratitude.

Above these are special acknowledgments to my lovely sisters Kgadi and Malebo for the consistent motivation, silly jokes and moral support; To my beloved Shirley Rambau, for always being around, rendering your home my writing resort, being patient with understanding in my absence and tirelessly pushing me to meet the mark on time and on bar; Thank you Queen. To friends Gaopalelwe Motaung, Duduetsang Kgomotshwane, Matome Maloba and Katlego Sebopela for being great academic companions in this long run, and to Okgonne Maloka and Uncle Lukas for your constant support.

Acknowledgements to the Masekane clan, to the Zion Christian Church and spiritual leader His Grace The Right Reverend Bishop Dr. B.E. Lekganyane and Baruti for the rendered spiritual counsel in the lead up to the completion of this work; in the name of God through our Lord Christ I humbly thank you.

Finally and above all; To God of great Heaven, for the opportunity, the strength, the Music, the will and eagerness in me to learn, to work and to fight, rendering the successful completion of this project; with all I humbly thank you.

To the reader, may this work in its contribution to science serve you well in mankind’s quest to seek knowledge, and may peace be unto you.

Dedication

To my parents, Nakampe and Dikeledi, for all the hard work they have invested in me.

Table of Contents

List of Acronyms

IBA	-	Ion Beam Analysis
SIMS	-	Secondary Ion Mass Spectroscopy
LABS	-	Laboratory for Accelerator Based Sciences
PIXE	-	Particle Induced X-ray Emission
HI-PIXE	-	Heavy Ion Particle Induced X-ray Emission
RBS	-	Rutherford Backscattering Spectroscopy
XRF	-	X-ray Fluorescence
SRIM	-	Stopping and Ranging of Ions in Matter
PWBA	-	Plane Wave Born Approximation
ECPSSR	-	Energy loss (E) and Coulomb deflection (c) of projectile ions and Perturbed-stationary state (PSS) and relativistic nature (R) of the atom
VIBA	-	Virtual Ion Beam Analysis
OMDAQ	-	Oxford Micro-Beams Data Acquisition
MCA	-	Multi-Channel Analyzer
ADC	-	Analog to Digital Convertor
TAMS	-	Tandem Accelerator Mass Spectrometry

List of Figures

List of Tables

Chapter 1

Introduction

1.1 Ion-atom collisions: X-ray production

The study of ion beam-matter interactions continues to be of interest for both fundamental physics and practical applications. When a beam of swift particles impinges on a material, a number of interactions take place, one of which leads to the production of X-ray photons [1]. These are produced as either bremsstrahlung (i.e. radiation produced due to the deceleration of electrons) and/or as characteristic X-ray photons where X-rays are produced as an atom electronically relaxes post the ionization of its electron shell(s). Due to the chemical specificity of electronically neutral element-atoms where the number of electrons in an atom is unique to a particular element, the energy of characteristic X-ray photons for particular electronic transitions is element specific [2]. Characteristic X-ray energies arise due to the difference in orbital binding energies of the electron shell from which an electron is ejected by an incoming projectile, and the shell to which an electron falls in its transition to fill up a created vacancy (by the ejected electron). This unique set of X-ray energies constitutes a spectrum of observable X-ray fingerprints from which individual elements can be identified.

Although this, in principle, is the case, the identification of elements from a particular atomic matrix and the subsequent approximations of elemental concentrations in matter is hindered by incomplete knowledge of the extent to which X-rays can be produced for ion induced emissions. The physical quantity which informs the estimation of such an extent is described by the X-ray

production cross section (i.e. the ion-velocity dependent probability of X-ray generation from an atom as a projectile ion passes through the vicinity of the target atom) [3]. This probability is described as a function of the ionization cross section (i.e. the ion-velocity dependent probability of inner-shell ionization by an incident ion) and the fluorescence yield which describes the extent of X-ray production due to the ionization and de-excitation of an atom by a single ion. Both the X-ray production and ionization cross sections are represented by a regional area of the atom measured in units of barns ($1x10^{-28}m^2$).

In the event of a collision between a projectile ion and a target atom, ionization can only occur if the incident projectile ion passes through this defined cross section region [1]. Although the relation between X-ray production and ionization is well defined, the X-ray production and the ionization cross section are not the same and not of the same value (i.e. different sizes of the two regions). This is because the occurrence of ionization may also induce another type of reaction, such as the non-radiative Auger effect (see chapter 2) [1]. It is therefore important to establish the X-ray production cross section relative to the ionization cross section (differential cross section) in order to estimate the extent to which a target atom may generate X-ray photons (i.e. the X-ray fluorescence yield) post an ion-atom collision.

1.1.1 Particle Induced X-ray Emission (PIXE) spectroscopy

Particle Induced X-ray Emission (PIXE) spectroscopy is an Ion Beam Analysis (IBA) technique wherein energetic ion beams are used to probe matter through the emission of characteristic X-ray photons from a material [2]. This is done through the detection and analysis of characteristic X-ray photons due to a number of electronic transitions, which are then used for multi-elemental characterization and quantification. The technique plays a vital role in a number of fields, such as

in agriculture, biotechnology, medicine, archeology, electronics and also nuclear and materials sciences [4 - 7]. The main contribution of PIXE to these industries is in providing non-destructive observations of trace elements and multi-elemental concentrations in fragile material samples [8].

Proton beam PIXE has been the mainstay of the PIXE technique since its inception in 1970[1]. The notion of the 'P' in PIXE being interchangeable between 'Proton' and 'Particle' was mainly due to the extensive use of protons in conducting PIXE analysis [1]. In tandem with experimental data, there has been a steady improvement in theoretical descriptions of ion-atom collisions leading to more accurate predictions of X-ray production cross sections.

The earliest of these, developed in the early 1980's were the Binary Encounter Approximation (BEA), the Semi-Classical Approximations (SCA) and the Plane Wave Born Approximation (PWBA) developed by Brandt and co-workers [9]. The PWBA, which had been most accurate compared to other approximations saw its modification and improvement by Brandt and Lapicki. These modifications resulted in a new approximation called the ECPSSR theory [10]. The ECPSSR theory has seen several modifications over the years since its first development in the mid 1980's, and describes differential cross sections for proton-target atom interactions fairly accurately compared to earlier theories. The availability of reliable theoretical cross sections by the ECPSSR theory for proton based atomic interactions has facilitated wide application of proton based PIXE spectroscopy to date in a number of scientific disciplines.

1.1.2 Heavy Ion Particle Induced X-ray Emission (HI-PIXE) spectroscopy

It has been experimentally observed in recent years that probing matter using heavier projectile ions results in a higher rate of emission of X-ray photons compared to those due to protons at the same velocity [11]. This suggests that Heavy Ion PIXE (i.e. PIXE conducted with heavy ions rather

than the conventional light ions (Z<3)) is more sensitive than proton based PIXE. An impeding factor in the implementation of Heavy Ion PIXE is that theoretical approximations which are used to predict differential cross sections cannot be simply extrapolated for heavy ion-atom based interactions [2]. This has been observed in comparisons of experimental data with predictions from the various theoretical approximations [3, 8, 10]. This is due to changing ion-atom collision mechanisms that occur due to heavy ions compared to protons. There is therefore a need for an extensive database of experimental cross sections to aid the development of theoretical formulations.

1.2 Ion beam analysis (IBA) at iThemba LABS

In South Africa, PIXE is one of the main Ion Beam Analysis (IBA) techniques found at the iThemba Laboratory of Accelerator Based Sciences (LABS). Ion beam analysis (IBA) describes a cluster of modern analytical techniques used for materials' analysis through ion beam-target interactions of a particular physical nature. These include the observation of ion-atom elastic, inelastic and nuclear reactions, as well as photon emission. The analysis of the different products of ion-atom interactions constitutes the various independent IBA techniques. In addition to PIXE, other IBA techniques include Particle Induced Gamma-ray Emission (PIGE) spectroscopy, Rutherford Backscattering Spectroscopy (RBS), Elastic Recoil Detection Analysis (ERDA), Nuclear Reaction Analysis (NRA) and MeV SIMS.

iThemba LABS is a South African multi-disciplinary research institution which houses laboratories in fields of environmental sciences, materials sciences and nuclear sciences. It is recognized as the largest accelerator based institution in all of Africa as well as the entire Southern hemisphere. It is an active participant in the international scientific community for low energy

physics experiments and also partakes in contributions to high energy nuclear physics based research. Ion Beam Analysis (IBA) is carried out by the Materials Research Department (MRD) in Cape Town, as well as the IBA department at the Tandem AMS facility in Johannesburg. This particular project forms part of an international collaborative effort between multiple research institutions in different countries, facilitated by the International Atomic Energy Agency (IAEA) where the collaboration aims to develop molecular concentration mapping techniques using MeV focused ion beams. Research on Heavy Ion PIXE, particular to this project forms part of the cluster of projects intended to achieve the underlined aim. The scanning nuclear microprobe beam line at the iThemba LABS 6MV Tandem accelerator is used to conduct PIXE and RBS analysis. This line has been used to conduct fundamental physical measurements such as heavy ion induced X-ray production cross sections for particular targets at non-destructive energies.

1.4 Aim and Objectives

The principle aim of this project was to contribute towards the global improvement of Heavy Ion PIXE spectroscopy through the measurement and publication of X-ray production cross section data for selected metallic oxide targets, compared with both the PWBA and the ECPSSR theory.

The objectives, in order to fulfil the underlined aim were to:

- Perform RBS characterization measurements on selected target films to be used for X-ray production cross section measurements.
- Perform X-ray yield measurements to determine X-ray production cross sections in V, Zr and Sn metallic oxide films due to ^{12}C and ^{35}Cl ion beams.
- Conduct a detailed comparison of experimental and theoretical ECPSSR and PWBA X-ray production cross sections due to carbon and chlorine ion beams.

1.5 Dissertation Outline

Chapter one serves as an introduction to the subject of the project by giving an overview of the basic theory for which the project is based, the background, history, the principal aim of the research study and concludes by underlining the objects from which the aim has been achieved. Chapter two covers the theoretical aspects of the subject of the project, thus expanding on the basic theory in chapter 1 giving insight into considerations of physical concepts taken into account in this dissertation. Chapter three as a continuum demonstrates how theoretical aspects discussed in chapter two are practically applied in experiment. This is done through a detailed description of the experimental setup of the scanning nuclear microprobe beam line used at iThemba LABS (TAMS) and also the acquisition of experimental data therefore. Chapter four discusses the results of the experimental data acquired and a detailed comparison with theoretical cross sections by the PWBA and the ECPSSR theory. Chapter five concludes the end of the dissertation by comprehensively stating the contribution of the work both in the South African and the international scientific context. This is done mainly through the highlight of the extent to which the aim and objectives of the project have been fulfilled, however ultimately the degree to which the principal aim of the study has been achieved in the project's contribution to the Coordinated Research Project (CRP) by the International Atomic Energy Agency (IAEA).

Chapter 2

Theoretical Overview

2.1 Introduction

X-ray generation in an atom induced by an incident projectile ion depends on a number of physical interactions that occur during an ion-atom collision. These physical concepts not only articulate the nature of particular ion interactions with matter which lead to the production of X-ray photons but also enable the description of the extent to which X-ray photons are and can be produced in matter. Chapter two serves as a theoretical overview of the main physical parameters used to describe ion-atom interactions; interaction potential, scattering, kinematics, ionization and X-ray production.

2.2 Ion-atom collisions: interaction potential

When an atom collides with an Ion of a given velocity and energy (eV), a number of physical interactions are bound to take place. These include processes such as forward and backscattering, elastic recoil, ionization and nuclear reactions. The prospect of a direct collision with the nucleus of the target atom is most improbable due to the extremely small size of the nucleus and relatively large distances to the surrounding electrons of its atom [12]. One other particular reason of this improbability is due to the positive charge of the nucleus which poses a Coulomb repulsion force in the case of positive incident ions and the negative Coulomb repulsive force in the case of negatively charged ions due to the electron cloud. At large distances between the incident ion and the atom, the positive charge of the nucleus is screened off by the negative electron cloud. The incident ion, as a consequence of screening, can only be repelled by the nucleus once it has entered the electron cloud of the target atom wherein the electronic screening effect is reduced as the ion

path inward the cloud increases. At this point of interaction, the mode of interaction between the projectile and atom depends on the energy of the projectile ion and the ion distance relative to the nucleus of the target atom. The energy required therefore to propel the ion about a certain distance from the nucleus is called the interaction potential, which implies that for every incident ion with a given energy, the size of the separation distance between the nucleus and the ion reduces as the energy increases and is increased as the energy is lowered. This relationship is described by an exponential function as shown by the figure below.

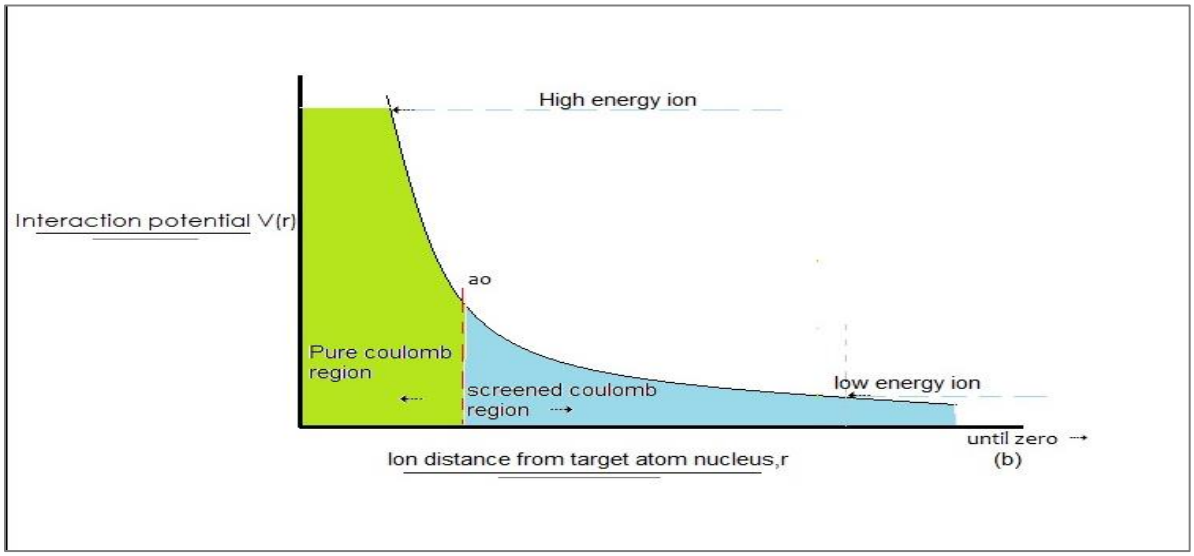

Figure 2.1. *Interaction potential plot of an atom. [12]*

The X-axis describes the ion distance **r** from the target atom nucleus. The ion distance from the nucleus can never be zero and is measured up to infinity [1, 12]. This is because for as long as an ion exists and is propelled towards a target atom, there is a given separation distance. In the case where the distance is extremely large, the interaction potential will be extremely low however existent even to the tiniest fraction. The pure Coulomb region describes the region past a point at which the screening effect of the electron cloud is non-existent, wherein only the positive Coulomb charge of the nucleus is experienced by an incident ion [1]. Figure (2.1) shows that high energy

ions are able to penetrate deep within a given distance from the nucleus past the screened Coulomb region. Low energy ions on the other hand only penetrate a small distance within the screened Coulomb region. Therefore, the interaction potential of an atom is important in describing how an ion sees an atom and thence interacts with it. For instance, in the case of high energy ions, the ion is able to pass through the screened Coulomb region and sees the atom as a small nucleus of concentrated positive charge, whereas a low energy ion sees its target atom as a relatively large sphere penetrable to a small limited depth. As the nature of ion-atom collisions is described by the interaction potential which is mathematically expressed by the general Coulomb potential, the following equation applies [13]:

$$V(r) = \frac{Z_i \times Z_A \times e^2}{r} \qquad ; for\ r < a_0 \tag{2.1}$$

where V(r) is the interaction potential, Z_i is the atomic number of the incident ion, Z_A is the atomic number of the target atom, r is the actual separation distance between the ion and the nucleus of the atom and a_o is the distance at which the pure Coulomb region of the target atom begins.

For low energy ions the screening function X(r) is included in the following equation:

$$V(r) = \frac{Z_i \times Z_A \times e^2}{r}.X(r) \qquad ; for\ r > a_0 \tag{2.2}$$

It is not easy to calculate the screening function, however, some numerical approximations (less than or equal to the value of 1) have been made and are available for specific ion-atom collisions [1].

2.2.1 Scattering

The impact parameter describes the closest distance of approach. This is illustrated using the figure below [1]:

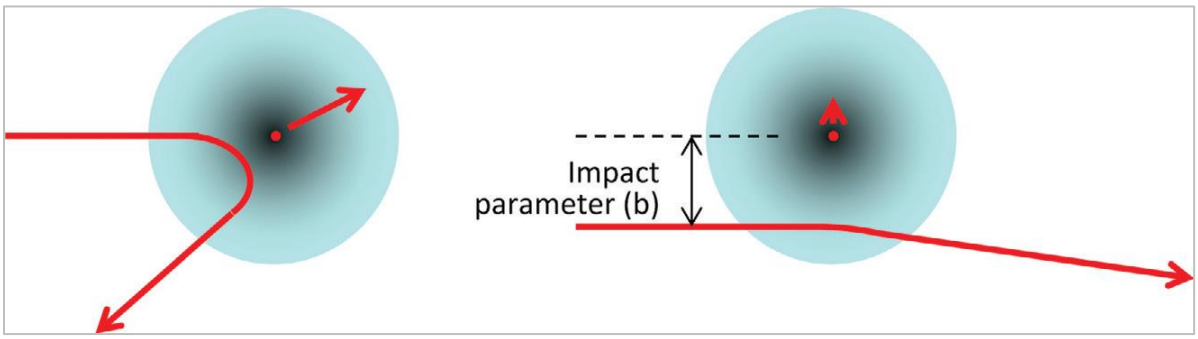

Figure 2.2 *Projectile impact parameter, with backscattering (left) and forward scattering (right) [1].*

The impact parameter is one of the factors that determine the type of scattering in ion-atom collisions. In the case of a relatively small impact parameter, as the ion distance from the target atom nucleus (r) becomes smaller, the ion will experience an increase in Coulomb repulsion from the nucleus as it travels deeper within the pure Coulomb region [14]. At the point at which the ion's kinetic energy completely diminishes along its initial ion path due to nuclear stopping, the ion will experience a large force at a given distance between the ion and the target nucleus. This force results in a large angle of deflection of the incident ion in the case where the ion is lighter than the target nucleus. This describes ion backscattering. When the impact parameter increases, the Coulomb repulsion force on the ion decreases as the ion travels further away from the nucleus. This leads to smaller deflection angles, thus resulting in what is referred to as forward scattering.

2.2.2 Collision Kinematics and energy transfer

In all ion-atom collision scenarios, there is a transfer of energy from the ion to the target atom. For elastic collisions such as in the case of back and/or forward scattering where it is assumed that no

energy is lost during the process of interaction, the mechanics of energy transfer between the ion and target atom can be described by the following equations [13].

$$E_1 = E_0\left[1 - \frac{4M_1M_2}{(M_1 + M_2)^2}\cos^2\varphi\right], \tag{2.3}$$

which is used to define the backscattering energy E_1 of the incident ion upon collision, and:

$$E_2 = E_0\left(\frac{4M_1M_2}{(M_1 + M_2)^2}\right)\cos^2\varphi\,, \tag{2.4}$$

which is used to describe the recoil energy E_2 of a target atom.

E_0 is the initial energy of the incident ion, M_1 and M_2 are the masses of the target atom and the incident ion respectively, and the angle φ is that of deflection.

The energy of the scattered ion or recoiled atom is dependent on the mass difference of the incident ion and the target atom. Therefore, for a particular ion of a certain energy, the energy at which the ion scatters will differ for every target element atom and similarly the energy of the various recoiled atoms will differ for every ion-element atom combination for the same ion and velocity [14]. Energy transfer therefore influences and describes the different types of ion-atom interactions and is hence important for understanding and predicting the type of interaction and reaction a particular ion-atom encounter might exhibit.

2.2.3 The Backscattering cross section

When an incident ion moves about the electron cloud of a target atom with a particular impact parameter, the probability of that ion to scatter either backward of forward can be determined for a known energy. The probability (cross section) of forward or backscattering of an incident ion depends on the trajectory of the ion relative to the perpendicular distance of the ion path from the nucleus of the target atom (i.e. the impact parameter). For a given ion-atom collision pair, the

backscattering cross section depends on the kinetic energy of the incident projectile, and thus its interaction potential. As there are variations in the impact parameter which influences the size of the reaction cross section; for experimental systems, the measurement of the backscattering cross section therefore depends on the angle of deflection of the ion by the target nuclei. The number of backscattered ions N_B is described by [15]:

$$N_B = \frac{\sigma_b \times N_i \times \Delta\Omega \times \Delta x}{\cos\theta} \tag{2.5}$$

where σ_b, N_i, $\Delta\Omega$, Δx and θ are the backscattering cross section, number of incident ions, detector solid angle, thickness of the target material and the scattering angle respectively.

This results in an angle dependent differential cross section wherein the number of incident particles are backscattered at an angle θ with a detector solid angle Ω (i.e. measured in barns per steradian). Equation 2.7 describes the backscattering cross section in a purely Rutherford potential [18]:

$$\frac{d\sigma}{d\Omega} = \sigma_R[mb/sr] \tag{2.6}$$

$$= 5.184 \times 10^6 . \left(\frac{Z_1 Z_2}{E[KeV]}\right)^2 . \frac{\{(M_2^2 - M_1^2 \sin^2\theta)^{\frac{1}{2}} + M_2 \cos\theta\}^2}{M_2 \sin^4\theta . (M_2^2 - M_1^2 \sin^2\theta)^{1/2}}$$

where M_1 and Z_1 are the mass and nuclear charge of the projectile ion, M_2 and Z_2 are the mass and nuclear charge of the target atom respectively. θ is the scattering angle and E is the energy of the incident ion. σ_R is the differential or measured backscattering cross section in an experimental system.

It has been observed for some (experimental systems) that the backscattering cross section may deviate from its Rutherford value due to the screening effect of the electron cloud of the target atom. In order to correct experimental backscattering cross sections, a correction factor is thus

needed to normalize the effect of electronic screening. The correction factor **F** is therefore introduced [18]:

$$\sigma_b = F \times \sigma_R \tag{2.7}$$

The correction factor for scattering angles of the range $\theta > 90^o$ at energies generally used in ion beam analysis is generally low, typically less than 10%. However, for scattering angles of the range of $\theta < 90^o$ some approximations have been seen to deviate from the expected value of the Rutherford cross section. The approximation by Anderson *et.al* is most accurate for both scattering ranges, and therefore corrects the backscattering cross section fairly accurately [14]. This is described by:

$$F_{Anderson} = \frac{\left(1 + \frac{1}{2}.\frac{V_1}{E_{CM}}\right)^2}{\left\{1 + \frac{V_1}{E_{CM}} + \left[\frac{V_1}{2E_{CM}.\sin\theta_{CM}/_2}\right]^2\right\}^2} \tag{2.8}$$

The subscript CM indicates that the cross section is measured from the center of mass system, where E_{CM} is the energy at the center of mass system, from which the scattering angle is measured. given by:

$$\theta_{CM} = \theta - sin^{-1}\left[\frac{M_1}{M_2\, sin\,\theta}\right] + \pi \tag{2.9}$$

The increase in kinetic energy V_1 is described by:

$$V_1[keV] = 0.04873 Z_1 Z_2 . \sqrt{\left(Z_1^{\frac{2}{3}} + Z_2^{\frac{2}{3}}\right)} \tag{2.10}$$

The corrected backscattering cross section σ_b therefore is equal to the experimentally measured backscattering cross section corrected by the Anderson approximation, where F as shown in equation (2.7) becomes $F_{Anderson}$.

2.2.4 Non-Rutherford scattering

Pure Rutherford backscattering reactions occur when an incident ion scatters due to the Coulombic repulsion from the charge of the nucleus where the scattering angle is dependent on the impact parameter. However, when the incident ion has a high interaction potential such that it passes through the pure Coulomb region, the probability for such an ion to move closer to the nucleus of the target atom increases. Therefore, as the interaction potential of an ion increases, so does the likelihood for the ion to overcome the Coulomb barrier and move even closer to nucleus of the target atom, and in some cases react with the nucleus of the target atom [16]. The ion therefore scatters at a very close proximity to the target nucleus where it experiences a large repulsion force that counters its projectile kinetic energy. The backscattering cross section therefore deviates from the pure Coulomb region for high energy ions. The energy at which an ion passes the Rutherford region is dependent on the mass of the ion and is described by the following equations:

$$E_D = \frac{M_1 + M_2}{M_2} \times \frac{Z_2}{10} \tag{2.11}$$

where M_1, M_2, Z_1 and Z_2 are the masses of the ion and the target respectively and the respective atomic numbers of the ion and the target element atom.

This only applies for an ion of atomic number Z=1 (i.e. for proton beams).

For Z_1>1, the following equation applies:

$$E_D = \frac{M_1 + M_2}{M_2} \times \frac{Z1 \times Z_2}{8} \tag{2.12}$$

where E_D is the energy (MeV) at which deviations in the Rutherford backscattering cross section are expected for the respective ions.

2.3 Ionization and X-ray production

2.3.1 Direct Ionization

Ionization is a process in which an atom is turned into an ion as a consequence of electron loss or electron gain. One of the ways in which ionization occurs is through ion-atom collisions. When a projectile ion collides with a target atom; the energy of the incident particle can be transferred to the target atom's electronic system, causing an energy state of excitation of the target atom. This (excitation) entails the atom carrying excess energy, rendering an unstable state. The atom as a consequence, in order to relieve itself of this excess energy, will lose one or more of its electrons (depending on the amount of energy needed to be removed in order to regain stability) from its electronic system. This process describes the occurrence of direct ionization, wherein a formerly electronically stable atom exhibits a particular charge state after a projectile-ion impact.

In the context of particle induced characteristic X-ray production, the ionization of an atom from which X-ray photons are produced is due to the ejection of inner shell electrons of a particular target atom. The probability of the occurrence of electron shell ionization is measured by an ionization cross section which describes a regional area of probability measured in barns. This implies that electron shell ionization can only occur when an ion incident onto an atom passes within a certain area within the electron cloud of the target atom.

The ionization cross section σ_i in terms of the X-ray production cross section is given by the following equation [17]:

$$\sigma_i = \frac{\sigma_x}{\omega_K^0 \times P_i}, \tag{2.13}$$

where P_i, σ_x and ω_K^0 (for single hole vacancies) are the intensity of the X-ray photons arising from all possible transitions of the line 'i', the X-ray production cross section and the single-hole fluorescence yield (discussed later in the chapter) respectively.

2.3.2 Electron capture

The ionization of an atom as a consequence of ion-atom collisions may not only be due to direct ionization mechanisms where an electron is 'knocked-off' a target atom's electron shell post interaction with a projectile ion. This is because there are other types of interactions that occur during ion-atom collisions which can lead to ionization. One such interaction is called electron capture, which describes the ionization of an atom through the loss of its electron(s) due to the capture of electrons by an incident projectile ion [12]. This occurs due to charge exchange processes that take place as two atomic species collide wherein inner shell target electrons are stripped into vacant orbitals of a highly charged projectile ion. Ionization of a particular electron shell by electron capture is described as a function of the energy dependent probability of electron capture, called the electron capture cross section [18]. At given ion energies therefore, the total ionization probability may be significantly affected as a consequence of a high electron capture cross section. For radiative ionization events, the electron capture cross section is important in determining the reaction cross section, such as the X-ray production cross section described in section 3.6.1 of chapter 3.

2.3.3 Multiple Ionization

Multiple ionization describes an event in which more than one electron shell is ionized by one incident projectile ion [19]. This results in the creation of multiple vacancies within various principal and sub-electron shells of the target atom and thus the subsequent emission of multiple

X-ray photons as the atom de-excites. This implies a higher X-ray yield and therefore a higher probability of X-ray emission (an increased X-ray production cross section). The high ion induced electron deficiency results in a change in the orbital binding energies of the electron shells which are ionized during the ion-atom collision [19]. Simplistically, heavier ions which ionize more than one electron shell of a target atom induce a higher electron deficiency due to the large number of vacancies created when the atom‘s electron shells are ionized. This increase subsequently results in an increase in the known characteristic X-ray photon energies (see section 2.3.4.1. for the calculation of characteristic energies). The electron deficiency in particular electron shells reduces the negative Coulomb screening effect of the target atom. This creates ion induced polarization within the target atom [18].

For ionizations of the inner shells L-, M- and beyond (principal quantum numbers n>1), the Coster-Kronig and Super Coster-Kronig transitions (see 2.3.4.1) as well as the fluorescence yield can no longer be assumed to be due to single-hole ionization because of multiple vacancies/holes created. Furthermore, the electron capture cross section is affected and is most probable to increase [18, 20]. These effects significantly increase the X-ray production cross section which depends on the various physical mechanisms that are affected by Multiple Ionization.

This is due to an increased probability of electronic transitions (i.e. a process of atomic relaxation which occurs to stabilize the atom) that may occur between ionized principal and sub-shells due to the large number of vacancies created (multi-de-excitation process). As the electrons transition from their various shells to the various principal and sub-shell vacancies, the number of characteristic X-ray photons that will be emitted due to these transitions will be relatively higher for one heavy ion-atom collision compared to that of a proton-atom encounter of the same ion

velocity. The probability of X-ray emission will therefore have increased and thus an increased X-ray production cross section [21]. For heavier projectiles which have a higher likelihood of inducing a higher degree of multiple ionization, the X-ray production cross section as such is more likely to increase.

2.3.4 Atomic relaxation

2.3.4.1 Characteristic X-rays

When an atom in its excited state undergoes de-excitation, it exhibits a loss of energy in order to attain a stable state. The mechanism of this loss of energy is through photon and electron emission. For matter of a matrix comprised of a number of atoms, the photons emitted therein exhibit a continuous range of wavelengths from the electromagnetic spectrum. When an individual atom in the matrix of atoms undergoes photon radiative de-excitation that is non-screened by the photons emanating from its neighboring atoms during their process of de-excitation, the wavelength of particular photons emitted from such an atom are characteristic to the atom and therefore describe its structure.

Characteristic X-ray photons are one such an example. The energy of a characteristic X-ray photon is a result of the difference in orbital binding energies of the electron shells from which the ejected electron and the transitioning electron originate.

The characteristic energy of a photon emerging from an atom due to electronic transitions is described by the difference in electron shell orbital binding energies of the upper electron shell from which the transitioning electron originates, and the lower electron shell from which the vacancy originates:

$$E_p = E_{Upper} - E_{Lower} \tag{2.14}$$

The orbital energy, from which characteristic energies are determined, is dependent on the mass of the electron, the potential energy of the electron shell and Planck's constant, which relates the photon wavelength and frequency. For a proton atom with only one electron and one electron shell, the electron orbital energy is described by [22]:

$$E_O = -\frac{Z^2 \times me^4}{2(4\pi\varepsilon_0)^2 h^2 n^2} \tag{2.15}$$

$$E_O = -\left(\frac{me^4}{2(4\pi\varepsilon_0)^2 h^2}\right) \times \frac{Z^2}{n^2} \tag{2.16}$$

By analyzing the quotient of all known constant parameters m, π, ε_0, e and h; the orbital energy for the Bohr model of the atom is given by:

$$E_O = -(13.57eV) \times \frac{Z^2}{n^2} \tag{2.17}$$

The orbital energy in (2.17.) is applicable only to a hydrogenic atom. This is because heavy atom electrons in orbit (Z>1, which exhibit more than one electron in their electron orbits) are not all subject to the total positive charge of the nucleus as in the electron of a hydrogenic atom. This is due to the screening effect by the negative charges of neighboring electrons which 'screen out' or reduces the magnitude of the positive charge of the nucleus for which the individual electrons in orbit are subjected. This effect alters the potential energy due to changes in charge of the electron shell. To account for the change in charge ((Z - 1) e^2) due to the screening effect, the simplified modified orbital energy is given by [22]:

$$E_{Mo} = -(13.57eV) \frac{(Z-1)^2}{n^2} \tag{2.18}$$

For X-rays produced due to the ionization of the K-shell (principal quantum number n=1), the X-rays produced can either be the K_{α}, K_{β} or K_{γ} for which all describe the particular electronic transitions from either the L- (n=2) or M- (n=3) shells [20]. The energies of the X-rays produced due to these various transitions differs with respect to the differential of the respective binding energies from which the vacancy and transitioning electron originate. The various possible electronic transitions are depicted by Figure 2.2:

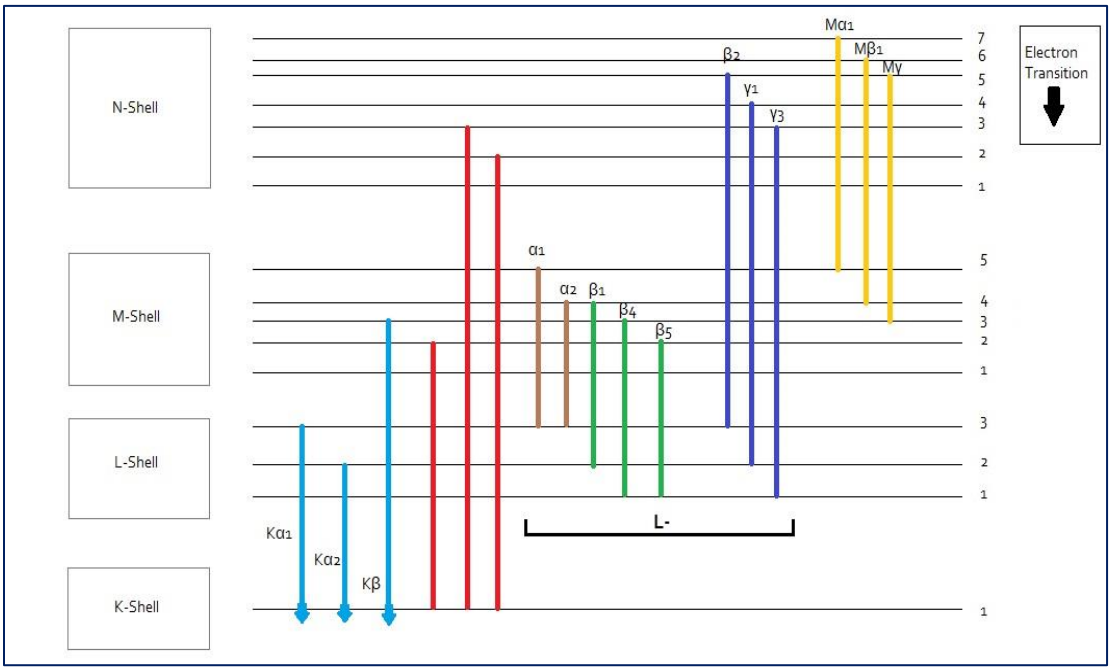

Figure 2.3 *Characteristic X-ray radiative electron transitions for the K-, L- and M- series. [15]*

Table 2.1. *Radiative characteristic X-ray electron shell transitions for the K-, L- and M- series. [12]*

X-ray photon	Electronic transition
Kα1	K-L3
Kα2	K-L2
Kβ	K-M3

Lα1	L3-M5
Lα2	L3-M4
Lβ1	L2-M4
Lβ4	L1-M3
Lβ5	L1-M2
Lβ2	L3-N5
Lγ1	L2-N4
Lγ3	L1-N3
Mα1	M5-N7
Mβ1	M4-N6
Mγ	M3-N5

Where the various electronic transitions depicted are described by the following:

$$\sigma_{X,K} = \sigma_{i,K} \times \omega_K \tag{2.19}$$

$$\sigma_{X,Ll} = (\sigma_{L1} f_{13} + \sigma_{L1} f_{12} f_{23} + \sigma_{L2} f_{23} + \sigma_{L3}) \times \omega_3 F_{3l} \tag{2.20}$$

$$\sigma_{X,L,\beta} = \sigma_{L1}\omega_1 F_{1\beta} + (\sigma_{L1} f_{12} + \sigma_{L2})\omega_2 F_{2\beta} + (\sigma_{L1} f_{13} + \sigma_{L1} f_{12} f_{23} + \sigma_{L2} f_{23} + \sigma_{L3})\omega_3 F_{3\beta} \tag{2.21}$$

$$\sigma_{X,L\gamma} = \sigma_{L1}\omega_1 F_{1\gamma} + (\sigma_{L1} f_{12} + \sigma_{L2})\omega_2 F_{2\gamma} \tag{2.22}$$

where F_n and f_n are Coster Kronig coeficients at the n shell.

Characteristic X-ray peaks (i.e. statistics of X-ray photon counts for a set of particular ion-atom interaction events over a specific amount of time) describe particular electronic transitions. Kα peaks for instance, describe the statistics of X-ray photons per given time due to electron transitions between L3 and/or L2 (upper orbits) and the K-shell (lower orbit). For an ideal experiment, the center of the peak describes the energy at which the most photons are produced for that transition series. The peak center therefore approximates the characteristic energy of a particular transition series, in this case, the K-series (particular to alpha transitions). (Figure 2.3) illustrates these transitions in terms of Vanadium K-shell X-ray peaks:

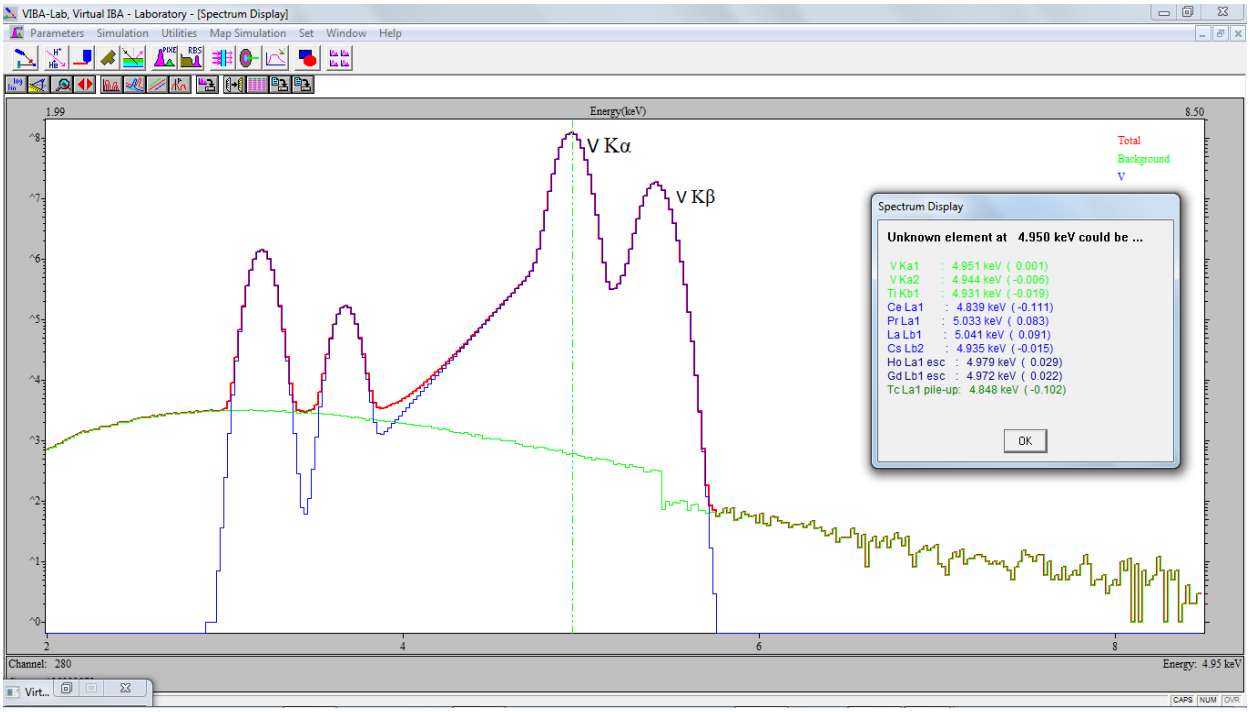

Figure 2.4 *Simulated PIXE spectrum using VIBA (Virtual Ion Beam Analysis) Lab for Vanadium X-rays due to K-series electron transitions induced by 2MeV protons [23].*

where the peak on the left (highest registered photon counts) represents X-ray photon counts due to Kα electron transitions and the smaller peak on the right (lowest registered counts) represents X-ray photon counts due to Kβ electron transitions.

2.3.4.2 The Auger effect

Although photon emission from an atom post the ionization of its electron shells is generally observed as the atom's tool for de-excitation in the context of X-ray production, there are however cases in which the de-excitation energy is transferred to an electron of the atom's outermost shell where the electron is ejected from the atom. This effect is called the Auger effect. The emitted electron is called the Auger electron, and its kinetic energy is equal to the difference between the energy change related to the electronic transition (i.e. of the electron filling up the vacancy) and the ionization energy of the electron shell from which the Auger electron is emitted [24]. Just as in the case of characteristic X-ray production, the energy of the Auger electron depends on the chemical structure of an atom in terms of the characteristic feature of its electronic system. The kinetic energy of the Auger electron therefore is characteristic of the atom element from which it is emitted [24].

When Heavy projectiles (Z>3) are used for ion-atom collision systems; due to the Multiple Ionization (MI) effect, the target atom tends to emit both an Auger electron and an X-ray photon by just one ion-atom interaction. This effect is called the Radiative Auger effect and is one of the most common observable features in the context of heavy ion induced characteristic X-ray production. Another of these MI induced features are special Auger transitions, which occur due to Coster-Kronig transitions. When an ionized atom relaxes due to electronic transitioning in a particular shell, the atom tends to emit an Auger electron from that particular subshell instead of an X-ray photon. In this case, the excess energy of the target atom is lost through the characteristic energy of the emitted Auger electron [11, 24].

2.3.4.3 X-ray fluorescence

During an ion-atom collision, the ionization of an electron shell which constitutes a single-hole vacancy can result in an event where characteristic X-rays amongst other photons are emitted to relieve the target atom of its excess energy. This event is called atomic relaxation where X-ray production refers to only one possible mode of this occurrence [25]. The measure of the extent to which an atom relaxes through X-ray production is described by X-ray fluorescence [17]. The X-ray fluorescence yield therefore is a quantitative description of the extent to which X-ray photons are produced due to the ionization of an electron shell by one projectile ion. For electronic transitions due to the creation of single-hole vacancies, the fluorescence yield 'ω_k^0 'is constant. The single-hole X-ray fluorescence yield can be expressed simply as the ratio of the number of X-ray photons 'N_{Xp}' generated in a target atom and the number of vacancies 'V_X' filled up during a de-excitation process for particular electronic transitions. The mathematical description of the single-hole fluorescence yield is stated by equation 2.23 [17]:

$$\omega = \frac{N_{Xp}}{V_x} \tag{2.23}$$

2.3.4.4. Multiple Ionization effects on the Fluorescence yield.

Equation 2.23 holds true particularly for proton induced X-ray production. On the other hand, in heavy ion collisions where there is Multiple Ionization (MI) wherein one incident ion is able to ionize more than one electron, produce multiple vacancies and initiate more than one electron transition; the number of X-ray photons emitted thereafter is not confined to one radiative transition and is dependent on the type of heavy ion used [11, 26]. This is because heavy ions induce a unique set of electronic transitions due to the different number of vacancies that are created as the various electron shells are ionized. More ionization events and subsequent X-ray

photon emission events will be expected due to impact by a heavier ion as it contains more electrons and therefore a higher probability of more complex electron interactions between itself and the target atom [18]. The heavier ion at a given energy carries more momentum than the lighter ion at the same energy, and hence the interaction potential of the heavier projectile will be higher. This also implies a higher effect of the electronic and nuclear stopping power on the heavier ion compared to the relatively lighter ion. Taking these effects of Multiple Ionization into account, the typical single-hole fluorescence yield described by (2.23.) cannot be assumed for heavy ion-atom X-ray radiative interactions. To account for Multiple Ionization effects on the fluorescence yield, in the case of K-shell X-rays, an approach by Tanis and co-workers [19] uses the following approximation of the fluorescence yield which takes into account X-ray and Auger transition rates:

$$\omega_K = \omega_K^0 \times \left[\omega_K^0 + (1 - \omega_K^0) \frac{\left[1 + \frac{I_{K\beta}^0}{I_{K\alpha}^0}\right] B}{1 + \frac{I_{K\beta}^0}{I_{K\alpha}^0} A} \right]^{-1} \tag{2.24}$$

where ω_K is the modified fluorescence yield, ω_K^0 is the single-hole fluorescence yield.

Constants A and B are functions of the V_{2p} and V_{3p} which are the number of 2p and 3p vacancies respectively. These are given by:

$$A = \frac{6 - V_{3p}}{6 - V_{2p}} \text{ and } B = 0.75 \times \left[\frac{R_{KLL}}{R_A} \left(1 - \frac{V_{2p}}{7}\right) + \frac{R_{KLM}}{R_A} \left(1 - \frac{V_{3p}}{8}\right) \right]$$

where R_A, R_{KLL} and R_{KLM} are the total, KLL and KLM Auger transition rates.

2.4 Theoretical X-ray ionization cross sections

The Plane Wave Born Approximation (PWBA)is one of the first theories to consider inner shell ionization and was derived from quantum mechanics. In this theory, the wave function of the

projectile is considered to be a Plane Wave (PW) and the emitted electron a hydrogenic wave. The theory owes its existence to the Born Approximation (BA). The BA states that the wave function of the projectile ion is not deformed by the potential of the target nucleus. Thus the PWBA describes a plane wave projectile which is not deformed by the potential of the target nucleus with the emission of an electron of a hydrogenic wave [10].

Similar to the Binary Encounter Approximation (BEA), the Plane Wave Born Approximation (PWBA) has been observed to be largely good in the qualitative sense [2]. In most cases however, the PWBA does not successfully reproduce experimental cross sections, especially due to heavier projectiles. This is because the PWBA does not correct for effects of coulomb deflection, energy loss and perturbation [15, 24]. The theory was seen to be off the mark at relativistic energies. A new theory based on the PWBA that corrects PWBA limitations was introduced by Brandt and Lapicki in the form of the ECPSSR theory [10]. The ECPSSR theory takes into account the Energy loss of the projectile ion (E) due to Coulomb deflection by the target atom (C), the Perturbation (P) of the target atom's electron shells in its Stationary State (SS) and also the Relativistic (R) nature of the target atom's inner electron shells [28]. K-shell cross sections of the theory are described by the following equation [10];

$$\sigma_{K,i}^{ECPSSR} = C_s(dq_{0s})F_s(Z) \times \sigma_i^{PWBA}(m^R(\xi_s)\eta_s, \zeta_s\theta_s) \tag{2.25}$$

where $C_s(dq_{0s})$ describes the coulomb deflection, $F_s(Z)$ the energy loss correction factor, $m^R(\xi_s)\eta_s$ and $\zeta_s\theta_s$ the relativistic and corrections to the binding energy respectively. These are given by;

$$\zeta_s = 1 + \left(\frac{2Z_1}{Z_s\vartheta_s}\right)(G_s - H_s) \tag{2.26}$$

And

$$m_s^R(\zeta_s) \cong \sqrt{(1+\beta Y_s^2)} + Y_s, \tag{2.27}$$

which is the relativistic mass.

The ECPSSR theory predicts experimental data relatively well at high energies, or as the ion beam energy (i.e. subsequent ion velocity) increases [29], and for collisions where $Z_1/Z_2 \ll 1$. This is different from the Semi-Classical Approximation United Atom (SCA-UA) theory, which exhibits predictions of higher accuracy for lower energies and fairly agrees with experimental data better as the energy decreases [1, 3]. The ECPSSR theory is currently the most widely used of all mentioned theoretical approximations. Most theory vs experiment investigations are thus comparisons of ECPSSR predictions to experimental data [9, 21, 24, 30].

Chapter 3

Experimental setup and data analysis procedure

3.1 Introduction

Micro-beam facilities are used all over the world for the investigation of atomic and molecular compositions of materials. Chapter 3 describes the experimental setup used to conduct PIXE and RBS measurements on selected target films for the determination of X-ray production cross sections as well as thin film target thicknesses. Furthermore, data acquisition and analysis software used to process raw data from the detection systems of the apparatus are discussed. Finally, the data analysis procedure used to extract X-ray production cross sections from experimental data is explained.

3.2. The Tandem accelerator setup at iThemba LABS (TAMS)

The Tandem accelerator at iThemba LABS (TAMS) is an electrostatic particle accelerator designed to reach a maximum terminal voltage of 6 Mega Volts (MV). The system accelerates particles from a SNICS ion source to a positive voltage terminal of the center of the machine and out to the various target stations that house a number of Ion Beam Analysis (IBA) techniques such as Rutherford Backscattering Spectroscopy (RBS), Particle Induced X-ray Emission (PIXE) spectroscopy, Time-of-Flight Heavy Ion Elastic Recoil Detection Analysis (HI-ERDA) and Nuclear Reaction Analysis (NRA). The accelerator system also has a Middleton type Cesium sputter ion source built through a collaboration between iThemba LABS and the Lawrence Livermore National laboratory for the application of Accelerator Mass Spectrometry (AMS) [30]. X-ray production cross sectional measurements were conducted through PIXE and RBS

measurements on the scanning nuclear microprobe beamline for ion beams originating from the SNICS and Duoplasmatron helium ion source. The main components of the accelerator system and target end station are described below.

3.2.1. Ion Source

The Ion source used is an 860C SNICS source which uses Cesium sputtering for the production of negative ions [32 - 34]. The source consists of a Cesium reservoir, also referred to as an oven, which is used to heat up the solid Cesium metal contained within it. As the reservoir heats up, the Cesium metal evaporates into the enclosed vacuum region of the ion source. The gaseous Cesium condenses onto a cathode thus referred to as a 'cold cathode'. Some of the Cesium gas is ionized by a heating and ionizing surface (ionizer). As the positively charged Cesium ions are boiled off, they are accelerated toward the cold cathode which contains a target powder of a particular material (depending on the ion beam required). The interaction between the accelerated positive Cesium ions and the powder results in the sputtering of target atoms from the powder by the Cesium ions.

In this work, graphite and a silver chloride powder was used for the production of MeV Carbon and Chlorine ion beams respectively.

The sputtered atoms from the powder material gain electrons as they penetrate through the layer of the deposited condensed neutral Cesium on the surface of the cold cathode and hence become negative ions. Due to the low KV (Kilo Volt) operational ground potential of the SNICS source and the negative potential at the cathode from which atoms are sputtered, the sputtered negative ions are accelerated easily out of the source. An extractor positioned at the exit point aperture of the source with a positive potential range of 0-25 KV attracts the ion beam from the source. The

negative ion beam at this stage is then injected into the accelerator beamline and the Tandem accelerator tank [31]. Figure 3.1 shows a schematic diagram of the SNICS ion source highlighting the main components:

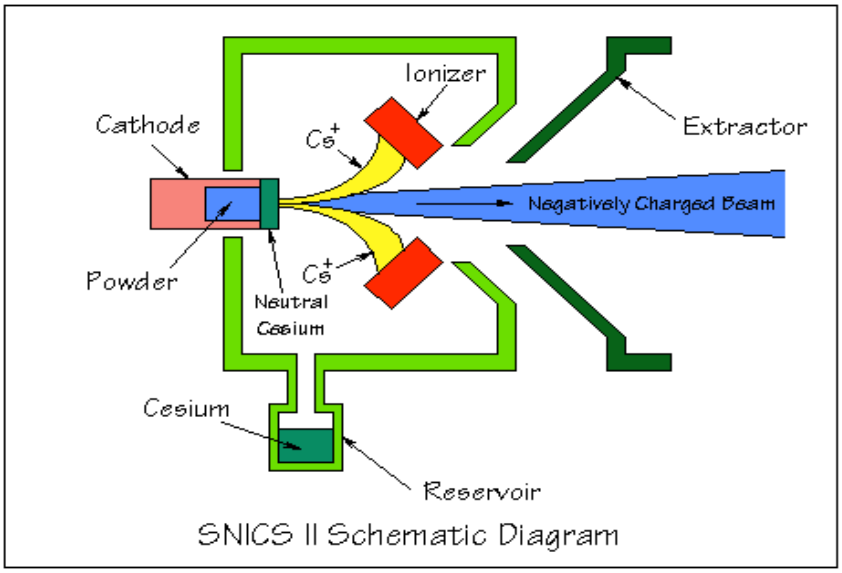

Figure 3.1 *A schematic of the SNICS ion source showing the main parts of the source [33].*

3.2.2 High voltage terminal

The negative ion beam accelerates from the ion source and passes through a series of ion optics which use magnetic fields to filter, shape and position the ion beam within the vicinity of the ion beam line. The attraction of the beam of negative ions by the positive terminal of the tank is the primary acceleration mechanism of the ion beam from the ion source and thus constitutes ion beam injection into the accelerator tank.

3.2.2.1 The Pelletron chain

The generation of the high positive potential in the accelerator tank is done through the transfer of charge by a pelletron chain. This chain consists of conducting metallic pellets connected to each other by an insulating medium. The chain is driven and revolves within the accelerator tank [35].

Similar to the Van de Graaff rubber belt of an electrostatic generator used to carry charge from one end to the other; a pelletron chain does the same, however with an improved charge collection efficiency due to the high conductance of the metallic pellets. The accumulated charge is deposited at the center of the tank where a high voltage potential builds up. A series of resistors are used as potential dividers in order to enable drawing out for use a selected specific potential instead of the maximum 6MV. Nitrogen gas and carbon dioxide (N_2 and CO_2) are pumped and kept at a pressure of 6-12bar in the tank as an insulator medium. This is done to prevent phenomena such as sparking, humidity build up, etc [35]. The velocity to which an ion beam is accelerated is dependent on the selected terminal voltage and the charge state of the constituent ions of the ion beam (2.6). Figure 3.2 shows a schematic of a sectional view of the tandem accelerator tank and the components mentioned herein:

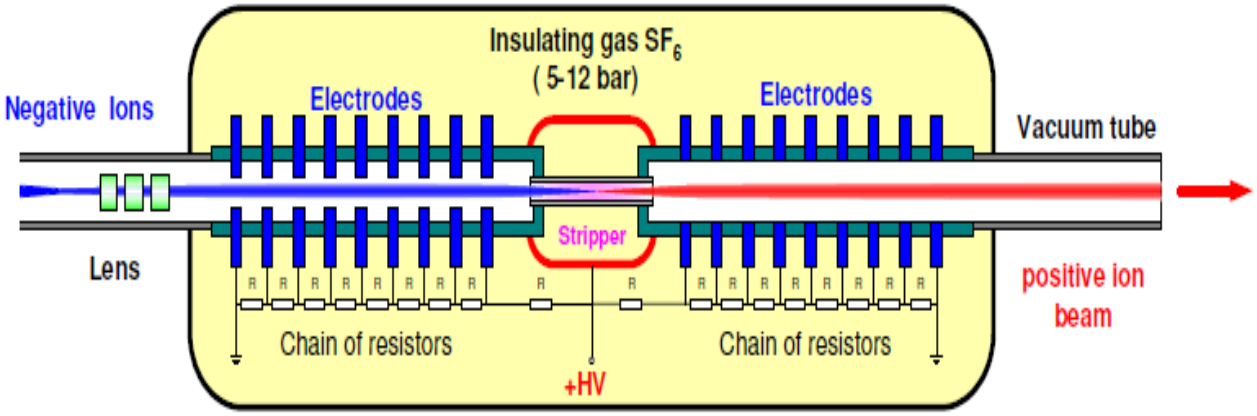

Figure 3.2. *Sectional view of a basic Van de Graaf Tandem accelerator. [35]*

3.2.4 Electron Stripping

Once in the tank, the beam passes through a stripper canal situated at the center of the high voltage tank. Therein electron stripping takes place where the negative ion beam is ionized (i.e. 'stripped' of its electrons). This is due to the direct interaction between the negative ions and the argon gas

(maintained at a pressure range of 10^{-3}-10^{-5} Torr) pumped into the stripper canal. The ion-atom collisions between the incident beam of negative ions and the atoms (Ar) of the stripper gas result in charge exchange processes between the ions and the atoms respectively [13]. The change in ion charge states and the distribution of charge therefore is due to electron-capture and electron-loss processes which occur as a consequence of the ion-atom collisions that take place. These processes are mathematically described as follows:

Electron-loss [35]

$$X_Z^q \rightarrow X_Z^{q+1} + e^- \tag{3.1}$$

where on the other hand, the equation that describes electron-capture is described by [35]:

$$X_Z^q + e^- \rightarrow X_Z^{q-1} \tag{3.2}$$

Overall ion beam stripping therefore is due to multiple events of electron-capture by target atoms of the stripper gas and electron-loss by the incident negative ions as a consequence of the subsequent ion-atom collisions between the two respective atomic species [36]. The injected beam of negative ions originating from the ion source does not carry a uniform and single charge state for all constituent negative ions. This is due to a uniform interchange of electrons between the Cesium and the target matter from which ions are sputtered during ion beam production [34]. The interchange of electrons between the injected beam and the stripper gas during their interaction will thus not bear an emergent ion beam of a uniform and singular charge state. The emergent mono-elemental positive ion beam therefore is constituted of ions of a number of different charge states.

The ejection of the ion beam from the accelerator Tank follows the stripping of electrons of the ion beam where the stripped positive beam is repelled by the positive potential of the terminal. The

mechanism of acceleration by a Tandem accelerator is thus of a pull (attraction) and push (repulsion) system.

3.2.3 Ion optics

Ion optics is an essential component of particle acceleration, as it enables the ability to focus, shape and steer an ion beam along its path. Ion beams typically emerge from an ion source widely spread and divergent. This is because ions are sputtered at the different angles. The mass analyzed ion beam undergoes passes through a series of electromagnets useful for beam steering and focusing, and slits useful for ion beam shaping. The extent to which an ion beam is focused or steered by an electromagnet is dependent on the magnetic field strength the beam experiences from the magnet, and the charge state of the projectile ions. The variation of magnetic fields through applied current or voltage to the electromagnets allows for a precise selection of the extent to which an ion beam is bent or shifted (steering) along its reference axis within the beam line. The force (Lorentz force) therefore which is exerted upon a charged particle moving through a region of electric and magnetic fields is described by [37]:

$$\vec{F} = q\vec{E} + q\vec{v}\vec{B} \tag{3.3}$$

where q is the charge of the projectile ion, v is the ion velocity, E is the electric field strength and B the magnetic induction.

The relative spread of the ion beam can be altered (focused or expanded) using ion beam slits or Einzel Lens'. This is done along the beamline of the accelerator and also along the target station beamline(s). These magnet lenses are used to focus ion beams from the 860C SNICS,

Duoplasmatron (He^+) and Middleton type AMS Cesium sputter ion source post ion extraction from the source.

Bending and selecting Magnets

A bending magnet is used to bend ion beams along a desired radial trajectory. Also referred to as inflection Magnets, bending magnets are essential for selecting which ions should be injected to the accelerator tank or to a specific target station. When a charged particle is subject to a magnetic field, the charged particle which is perpendicular to the magnetic field moves along a circular path of a radius r determined by the momentum *p* of the particle [37]. This is described by:

$$B \times r = \frac{p}{q} \tag{3.4}$$

The product of the radius of the trajectory followed by a charged particle and the magnetic induction is called the magnetic rigidity. This is essentially the effect of magnetic fields on the motion of charged particles which also describes the resistance of charged particles to magnetic fields due to the momentum of the particles. This implies that particles of a higher momentum will have a high resistance to deflection due to a magnetic field than ions of lower momentum.

This indicates that bending magnets can also be used as mass spectrometers, as the radii of the circular trajectories of ions moving about a particular magnetic field will not be the same depending on the various momentum of the different ions. For heavier ions with consequent higher momentum, the trajectory about the magnetic field will follow a larger radial track compared to that of a relatively lighter ion. This means that bending magnets can be used to 'select out' ions as they exit the magnet by having the desired ions bend at a radius that will have them emerge into a selected beamline [35, 37]. These type of magnets are called mass analyzing magnets or inflection

magnets and are placed at the exit point of the ion source and/or tandem accelerator. As the process of ion sputtering at the ion source and also electron stripping in the stripper canal of the tandem accelerator tank may exhibit an ion beam constituted by different elements, inflection magnets are necessary for selecting out a mono-elemental ion beam to emerge to a particular target station. Figure 3.3 illustrates how a bending or inflection magnet is used at the exit point of an accelerator tank emerge to a beamline leading to a desired target stations:

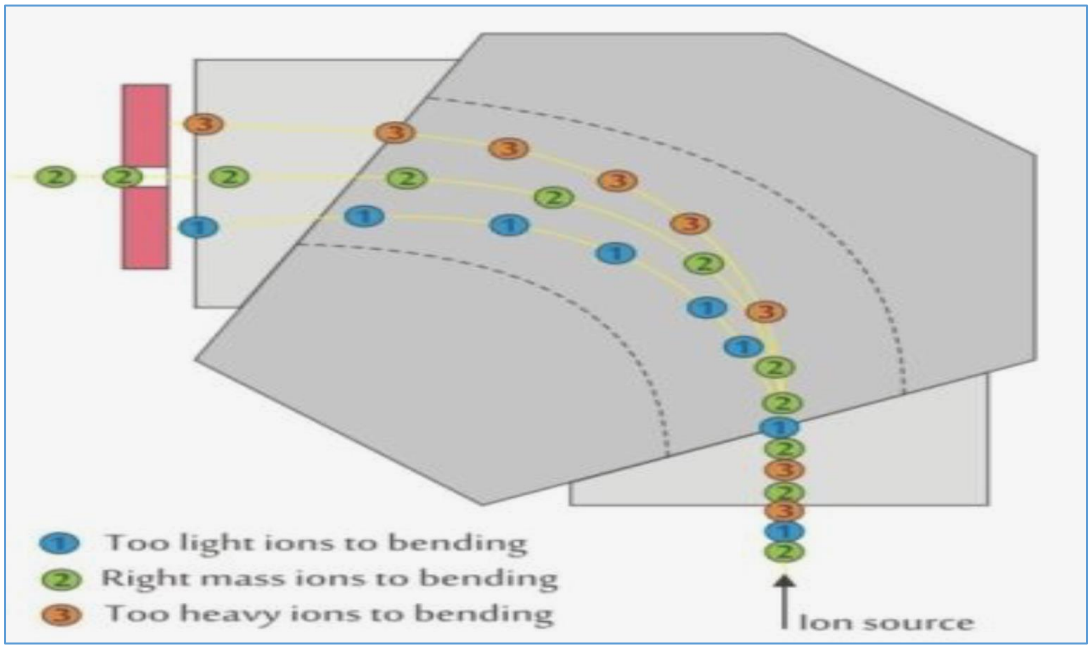

Figure 3.3. *Schematic diagram of a mass analyzing magnet. [35]*

3.3 Target stations

A schematic sketch of the floor view of the Tandem accelerator is shown by Figure 3.4:

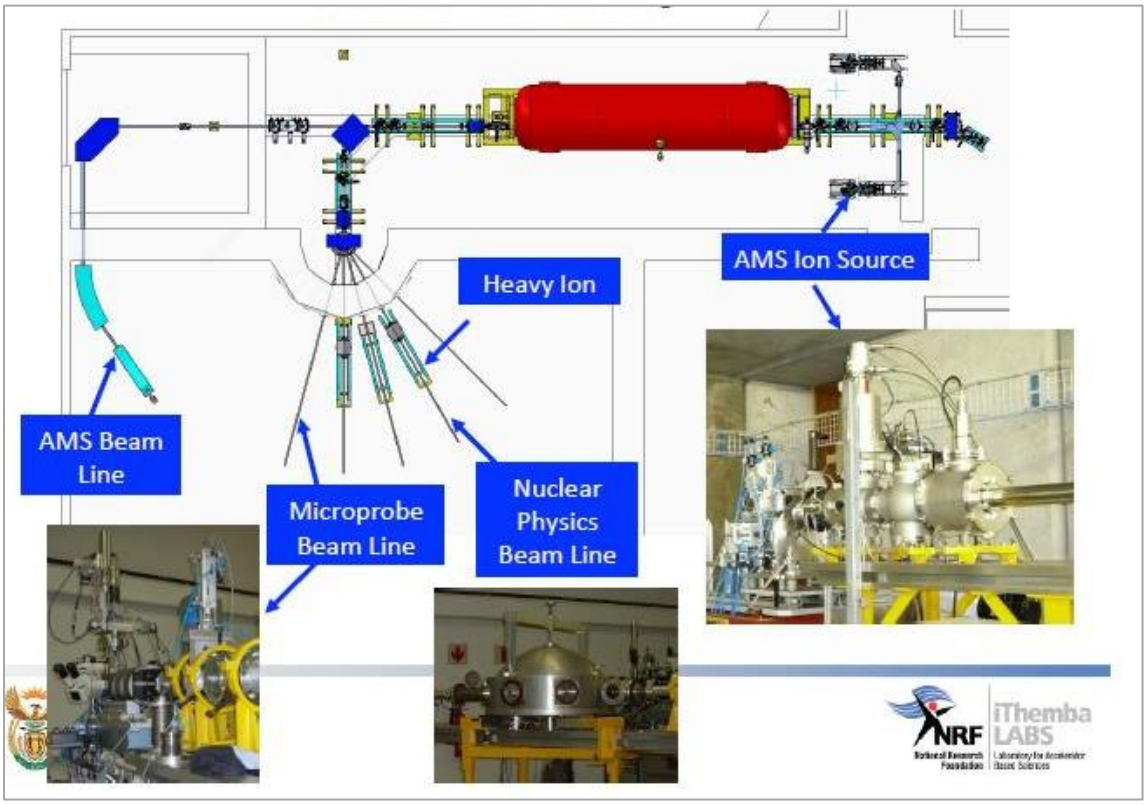

Figure 3.4. *Layout of the Van de Graaf Tandem accelerator facility at iThemba LABS (TAMS). [31]*

The Tandem accelerator at iThemba LABS (TAMS) houses three active target stations, namely the Heavy Ion Elastics Recoil Detection Analysis (HI-ERDA) and Nuclear Reaction Analysis (NRA) beam line, the scanning nuclear microprobe beam line and the Accelerator Mass Spectrometry beam line (AMS). There is a fourth IBA target station currently under construction. The selection angles for the three IBA target stations are described by the following table:

Table 3.1 *Selection angles of the switching magnet at the Tandem Accelerator facility (iThemba LABS (TAMS)).*

Target Beamline	Selection angle (^{0})
HI-ERDA, NRA beamline	30 east
Scanning nuclear microprobe beamline	15 west
Beamline in construction	0

Measurements to determine heavy ion beam induced X-ray production cross sections were done in the scanning nuclear microprobe target chamber, which is described below.

3.3.1 Scanning nuclear microprobe

Ion beams emergent from the tandem accelerator steered at an angle of 15^o west are delivered to the scanning nuclear microprobe target station at the end of the beam line. A copper slit is used to change the shape of the incident ion beam. Adjustments to the slits are done so as to vary the shape and size of the beam using micrometer screw gauge handles that measure the extent to which the slits are inserted or extracted from either one of the three ends of entry. The three entry points are on the left, right and top ends of the beam line.

A steering magnet, used to steer the emergent ion beam is mounted after the slits along the beamline of the microprobe. A Faraday cup is positioned before entry to the microprobe target chamber where it serves a dual function of measuring the ion beam current and also impeding the beam from reaching the target chamber. This is useful for ensuring safe levels of beam current for PIXE and RBS measurements that are non-destructive to the target material. A scanning magnet

is placed at the entry of the target chamber. The scanning magnet is used to cater for the movement of ions along the X and Y axes. This is useful for the examination of material surfaces and atomic structures. Ion beams can be focused using an electromagnet of a particular number of poles. The most commonly used are the Dipole, Quadrupole, the Hexapole and the Octopole which can be placed in a particular sequence (i.e. Singlet, doublet, triplets etc.) to meet the attributes of the required experimental setup [32]. For the purpose of obtaining microbeams at the scanning nuclear microprobe's target chamber, quadruple triplets are used. Figure 3.5 shows a picture of the scanning magnets and quadruple triplets of the scanning nuclear microprobe:

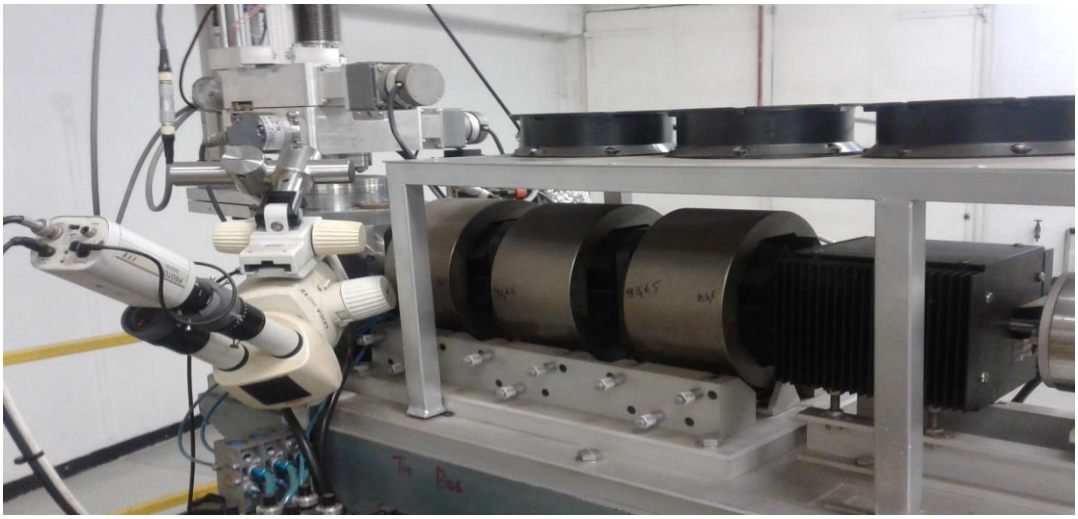

Figure 3.5. *Image of the scanning magnets and quadruple triplets of the scanning nuclear microprobe.*

PIXE and RBS detector setup

The target chamber is an octagonal steel high vacuum chamber (10^{-6} Torr) that houses the RBS and PIXE detectors. Samples are mounted onto a hexagonal steel sample holder that rotates at intervals of 60^{o} and so can hold six large area samples. A charge integrator is connected to the sample holder and is used to measure the ion beam current and collected charge. A Si(Li) detector (SDD) of solid angle 16msr is used to detect X-ray photons generated from the target sample. It

has a nominal resolution of 137eV FWHM at 5.9keV and mounted at an angle of 135^{o} from the incident beam direction (0^{o}) and at a distance of 50mm. For our measurements, a 15μm thick Mylar filter was placed on top of the 8μm thick Beryllium window of the Si(Li) detector to prevent a high influx of backscattered ions into the detector. The number of backscattered ions were counted by a Canberra PIPS detector of a solid angle of 46.2 msr at an angle of 150^{o} from the 0^{o} incident angle and at a distance of 57 mm away from the target sample. Both the Si(Li) and Canberra PIPS detectors were connected to a 0.45V per μC pre-amplifier with a gain of 20mV per MeV and an amplifier with a super fine gain of resolution better than 1 in 16000. The Si(Li) detector, connected to the first channel (0) of the Analog to Digital Converter (ADC) from the amplifier; and the Canberra PIPS detector, connected to the second channel (1) of the ADC from the amplifier were both connected to the Multi-Channel Analyzer (MCA) which is in-built to the data acquisition system (DAQ). Figures 3.6 and 3.7 Shows a schematic diagram of the detector setup(s) of both the Si(Li) and Canberra surface barrier RBS detector.

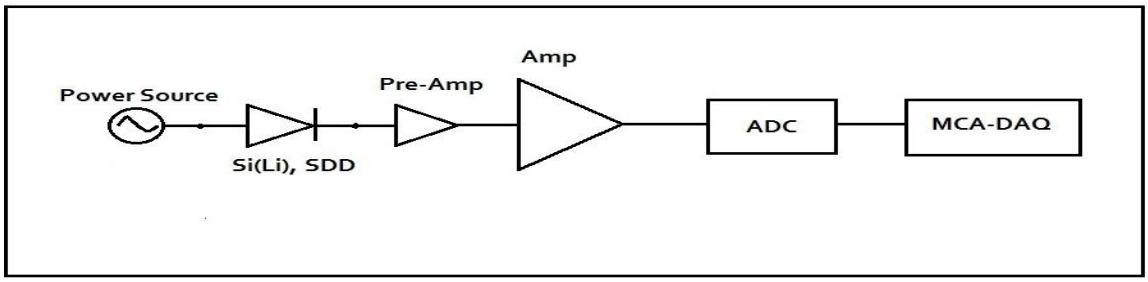

Figure 3.6. *Schematic diagram of an X-ray silicon detector.*

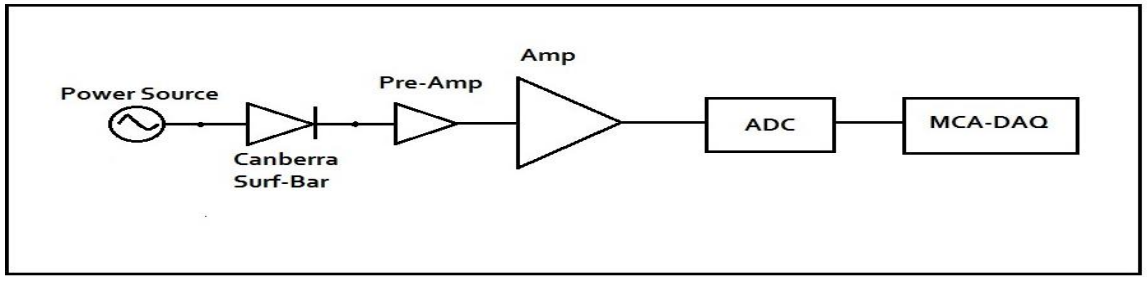

Figure 3.7. *Schematic diagram of an RBS Canberra surface barrier detector.*

Figures 3.8 and 3.9 Show images of the motorized sample holder and the two detectors inside the chamber respectively.

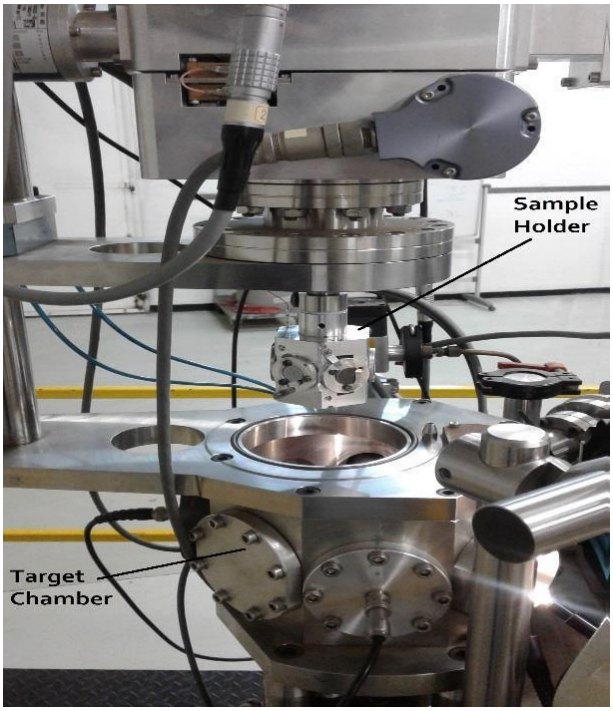

Figure 3.8. *Image of the target material sample holder connected to the motorized handler used to move the sample holder on an X- and Y- axis.*

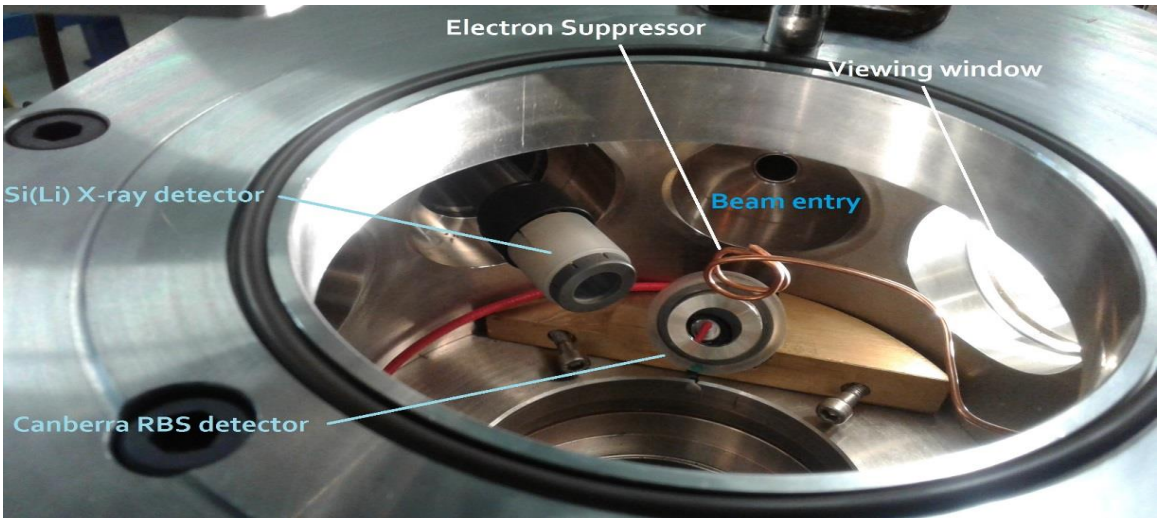

Figure 3.9. *Image of the scanning nuclear microprobe target chamber.*

3.4. Data acquisition and analysis software

3.4.1. OMDAQ

Oxford Micro-beams Data Acquisition (OMDAQ) 3, a C++ based software, was used for the dual acquisition of X-ray and backscattered ion counts signals from the ADC during experimental runs [32]. Furthermore, the accumulated ion beam charge from the charge integrator was measured and recorded for each experimental run. OMDAQ 3 is also used for the control of the automated motorized sample holder which can be adjusted to move in four directions (up, down, left and right). OMDAQ also enables a live view of the sample in the chamber though a live video feed from a mounted video camera positioned next to a viewing window into the target chamber. Figure 3.10 Shows the Graphical User Interface (GUI) of a PIXE and RBS spectra acquired through OMDAQ.

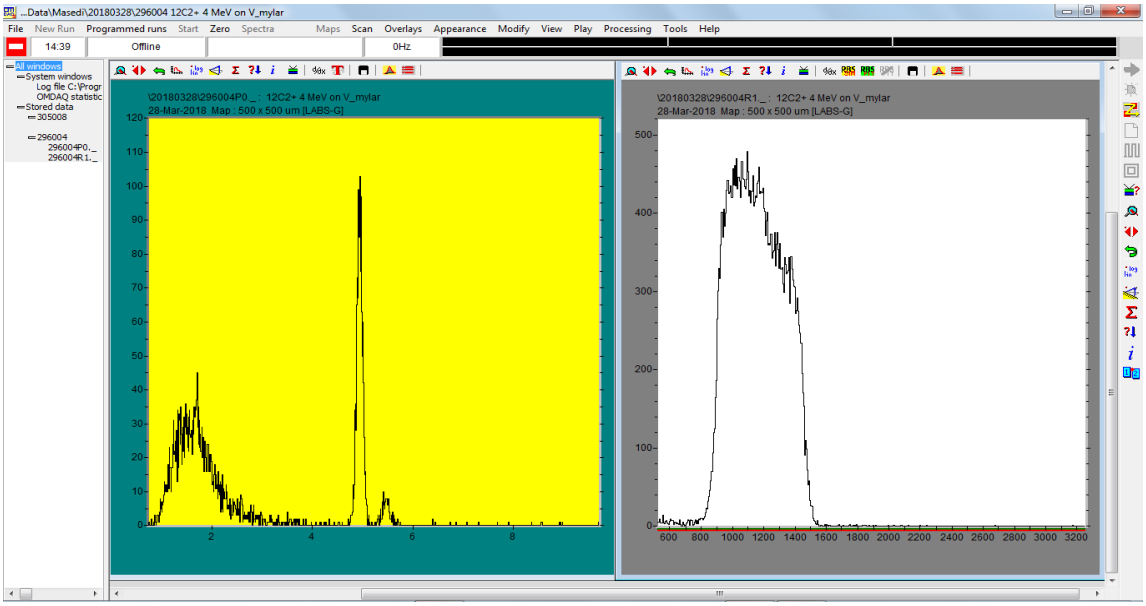

Figure 3.10. *Graphical user interface of OMDAQ showing PIXE (left yellow background window) and RBS (right white background window) spectra.*

The video live feed in OMDAQ is obtained from the following video camera mounted microscope from the viewing window of the target chamber of the scanning nuclear microprobe:

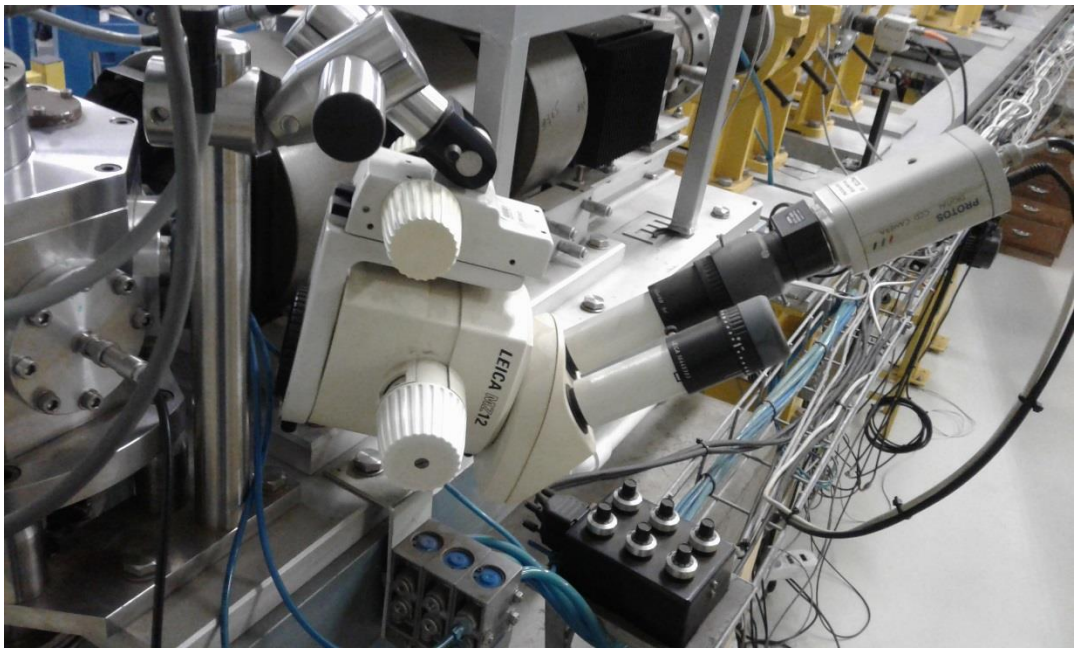

Figure 3.11. *Image of the video camera-microscope mounted target chamber viewer.*

3.4.2. SRIM

Stopping and Ranging of Ions in Matter (SRIM) is a software which is used to simulate the range of ions as they are implanted into a material(s) [16]. This takes into account the electronic and nuclear stopping powers of target atoms as they collide with incident ions. These energy dependent stopping powers are contained in a database hosted by the software for various ion-atom interactions. SRIM is therefore useful for predicting how far an ion of a particular energy will travel in matter. It is also useful for drawing from its database a table of stopping powers for ion-atom interactions at a particular energy range. Figure 3.12 Shows a Graphical User Interface of the SRIM input window for stopping power calculations and the table of results (output) therefore.

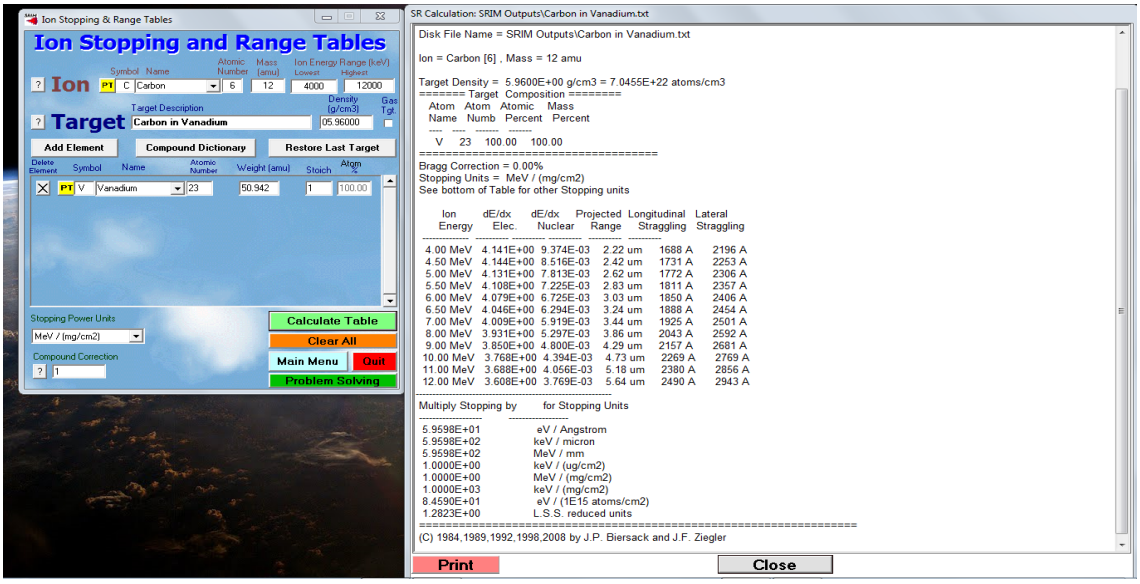

Figure 3.12. *Graphical User Interface of the SRIM input (left) and output (right) window for stopping power calculations.*

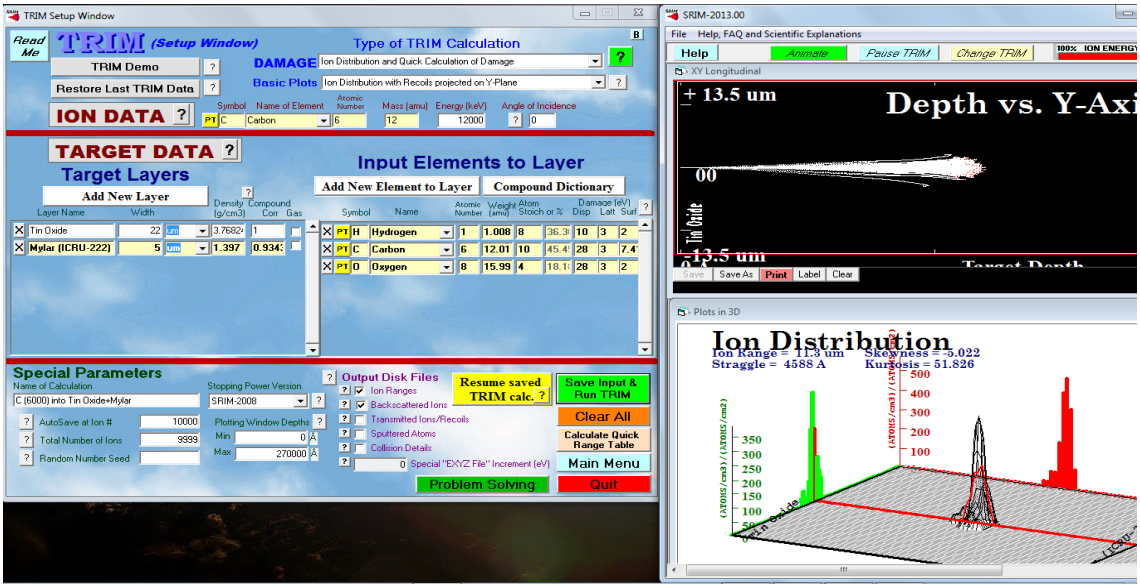

Figure 3.13. *Graphical User Interface of the SRIM Trim input window (left) and output window (right) for ion ranging in matter.*

In this work, SRIM was used for calculating stopping powers of heavy ions in matter needed for the determination of heavy ion induced X-ray production cross section energy loss corrections, as described in chapter 4.

3.4.3. SIMNRA

SIMNRA is a data analysis software that uses a database of Rutherford and non-Rutherford backscattering cross sections in order to simulate an RBS spectrum of a particular ion-atom backscattering interaction [14]. The simulated spectra is then used to overlay/fit over the acquired experimental RBS spectrum. The simulated spectra, corrected for the experimental spectra is then used to determine parameters such as the target layer thickness and stoichiometry.

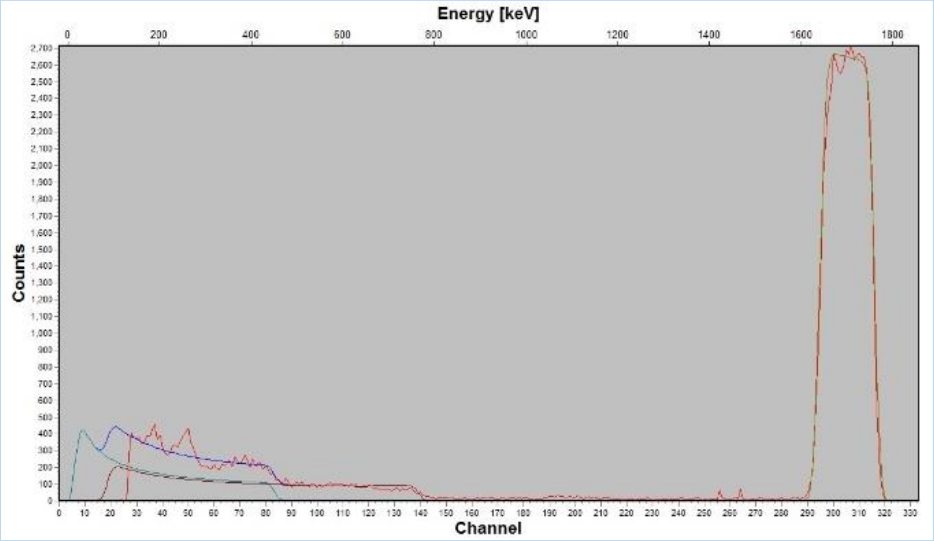

Figure 3.14. *Graphical User Interface of an RBS spectra analyzed using SIMNRA [Experiment for 2MeV He^+ in Sn oxide on Mylar].*

In this work, target samples were characterized by RBS using 2MeV He^+ ions. Target layer thickness and stoichiometry were then obtained through SIMNRA simulation. Results thereof are given and discussed in chapter 4.

3.5. Physical limitations

Certain physical limitations were encountered in the measurements carried out for this work. These are described hereunder.

The evaluation of the experimental X-ray production cross section described here relies on the accurate knowledge number of number incident ions in terms of the number of backscattered ions or the accumulated ion charge and ion charge state (2.3.5.). This evaluation in terms of backscattering is possible through dual PIXE and RBS analysis [1]. Although this is possible on the scanning nuclear microprobe, the evaluation through ion charge has been observed not to be possible. This is mainly due to the inability to get an accurate measurement of charge, possibly due to incomplete charge collection from poorly conducting samples. This inhibited the evaluation of X-ray production cross sections due to high Z number heavy ion-atom collisions where the probability of ion backscattering is too low for the observed backscattering counts to be relied on.

The Van de Graaff Tandem accelerator in practice, operates at a voltage potential range of 800kV-6MV. This implies a minimum energy of 1.6MeV for proton beams. Although this was sufficient for a number of experimental investigations, PIXE and RBS analysis could not be done at low energies (keV range) which could have been useful for observing low energy ion-atom interactions and consequent ionization mechanisms.

3.6 Data analysis procedure

3.6.1 Evaluation of X-ray production cross sections

The probability of X-ray photon generation in a target atom is described by the X-ray production cross section. For inelastic ion collisions, this cross section (measured in barns) describes the probability of emission of X-ray photons as an incident projectile ion passes through a particular region close to the target atom. This probability is dependent on the energy of the incident projectile ion and hence the X-ray production cross section varies as the energy changes for each particular projectile ion.

As the number of X-ray photon yields is given by ionization events due to incident ions, X-ray production is directly related to the number of incident ions [1, 2, 21];

$$N_X = \sigma_X \times \frac{N_i \times N_A \times \varepsilon \times \beta \times \Delta x}{A \times F(\Delta E)} \tag{3.5}$$

In this work this number (N_i) of incident ions in an ion beam was determined through counting the number (N_B) of backscattered particles detected from the same target material at a certain angle [1, 13];

$$N_B = N_i \times \frac{\sigma_B \times \Delta x \times \Delta\Omega}{\cos(\alpha)} \tag{3.6}$$

which gives

$$N_i = \frac{N_B \times \cos\alpha}{\sigma_B \times \Delta x \times \Delta\Omega} \tag{3.7}$$

where N_B, σ_B, $\Delta\Omega$ = 46.17msr, Δx and α are the number of backscattered ions, the backscattering cross section, the detector solid angle, the thickness of the target sample and the exit angle.

Substituting (3.5) into (3.6) gives;

$$\sigma_x = \frac{N_X}{N_B} \times \frac{A \times \Delta\Omega}{N_A \times \varepsilon \times \beta} \times \sigma_B \times F(\Delta E) \quad (3.8)$$

For a particular target atom of atomic mass A, and fixed solid angle, the quotient ($A.\Delta\Omega/N_A.\beta\varepsilon$) will remain constant from one incident ion to the next. This quotient constitutes a non-changing parameter (K-factor) described by equation 3.8:

$$K = \frac{A \times \Delta\Omega}{N_A \times \beta \times \varepsilon} = \frac{N_B}{N_X} \times \frac{\sigma_X}{\sigma_B} \quad (3.9)$$

From this, the X-ray production cross section is defined:

$$\sigma_x = \frac{N_X}{N_B} \times K \times \sigma_B \times F(\Delta E) \quad (3.10)$$

It must be emphasized that equation 3.9 assumes that the X-ray attenuation coefficient β and the detection efficiency ε, which both are energy dependent, are not affected by the incident ion.

3.6.1.1 Heavy ion induced X-ray production cross sections

X-ray yields due to heavy ions are known to be higher than due to light ions such as protons due to the MI effect [38]. In other words, ionization due to the same number of light and heavy ions would result in higher emissions for heavy ion induced reactions.

The approach used in this work to determine heavy ion induced X-ray production cross sections was to compare X-ray yields due to 2MeV protons and heavy ions under the same experimental conditions. The comparison of X-ray yields due to heavy and light ions, to compare the X-ray production cross section, must therefore be based on the same number of incident ions. Since the number of incident ions in an ion beam are determined from the number of backscattered ions, N_B in equation 3.9 has to be normalized to the same number of incident ions.

The normalization factor for backscattered heavy ions is given by the following equation [21]:

$$n_f = \frac{N_i(p)}{N_i(HI)} \tag{3.11}$$

Substituting 3.6 for protons and heavy ions gives:

$$n_f = \frac{N_B(p)}{N_B(HI)} \times \frac{\sigma_B(HI)}{\sigma_B(p)} \tag{3.12}$$

n_f is then calculated using N_B counts from raw RBS spectra and σ_B values from SIMNRA calculations. Combining equations 3.9 and 3.11, the ratio of heavy ion to proton X-ray production cross sections gives:

$$\sigma_x(HI) = \frac{\sigma_x(p)}{N_x(p)} \times N_x(HI) \times n_f \tag{3.13}$$

The normalization correction factor n_f is calculated separately for every set of ion-atom interactions (i.e. for every X-ray yield gathered due to a particular energetic ion beam).

An alternative method for determining σ_X is through the accumulated beam charge Q. The number of incident ions is then determined in terms of ion charge given by:

$$N_i = \frac{Q}{n \times e} \tag{3.14}$$

This is substituted into the backscattering cross section equation:

$$\sigma_B = \frac{N_B}{N_i \times \Delta\Omega \times \Delta x} \tag{3.15}$$

To produce:

$$\sigma_B = \frac{N_B \times n \times e}{Q \times \Delta\Omega \times \Delta x} \tag{3.16}$$

By substituting equation (2.36.) into equation (2.27.), the X-ray production cross section is described in terms of the charge of the ion:

$$\sigma_X = \frac{N_X}{Q} \times \frac{A \times n \times e}{\varepsilon \times \beta \times \Delta x \times N_A} \tag{3.17}$$

This method was, however, not pursued because of inaccuracies associated with measurements of charge incident on samples that are only partially conductive such as the metallic oxide films used in this work.

3.6.2 Energy loss correction factor F(ΔE)

For relatively thick target materials, the incident ion loses its energy as it penetrates the target [16]. Due to the energy dependency of the X-ray production cross section, the energy loss of an incident ion leads to variations in the X-ray production cross section due to ions of a range of different energies from the initial ion energy. Due to this effect, the approach described above for calculating experimental X-ray production cross sections cannot be used as is for thick targets. To account for the energy loss effect on the X-ray production cross section, a correction factor (F(E)) has to be introduced.

The loss of energy by an ion in thick targets is due to the nuclear and electronic stopping of the target and is described by [16]:

$$S(E) = -\frac{dE}{dx} \tag{3.18}$$

where the negative sign signifies that energy decreases as the ion path increases. Rearranging and integrating both sides of equation 3.17 gives:

$$\int_{Ef}^{Ei} dx = \Delta x = \int_{Ef}^{Ei} \frac{1}{S(E)} dE \tag{3.19}$$

where Δx is the target thickness, E_i is the initial ion beam energy and E_f is the ion beam exit energy.

The correction factor F(E) is described as the ratio of the measured X-ray production cross section σ_m to the X-ray production cross section at the initial energy of the incident ion:

$$F(\Delta E) = \frac{\left(\frac{d\sigma}{d\Omega}\right)_m}{\frac{d\sigma}{d\Omega}_{Ei}} = \frac{\sigma_m}{\sigma_i} \tag{3.20}$$

where the measured X-ray production cross section taking into account the energy change from the initial energy E_i to the final exit energy E_f is given by [39]:

$$\left(\frac{d\sigma}{d\Omega}\right)_m = \frac{\int_{Ef}^{Ei} \frac{\frac{d\theta}{d\Omega}(E,\theta)}{S(E)} dE}{\int_{Ef}^{Ei} \frac{1}{S(E)} dE} \tag{3.21}$$

Therefore:

$$F(\Delta E) = \frac{\frac{1}{\frac{d\sigma}{d\Omega}_{(Ei)}} \times \int_{Ef}^{Ei} \frac{\frac{d\theta}{d\Omega}(E,\theta)}{S(E)} dE}{\int_{Ef}^{Ei} \frac{1}{S(E)} dE} \tag{3.22}$$

which therefore implies:

$$F(\Delta E) = \frac{1}{\Delta x \times \frac{d\sigma}{d\Omega}_{(Ei)}} \times \int_{Ef}^{Ei} \frac{\frac{d\sigma}{d\Omega}(E,\theta)}{S(E)} dE \tag{3.23}$$

Or

$$F(\Delta E) = \frac{1}{\Delta x \times \sigma_i} \times \int_{Ef}^{Ei} \frac{\sigma(E)}{S(E)} dE \tag{3.24}$$

From this equation, the quotient of the X-ray production cross section $\sigma_{(E)}$ and the stopping power S(E) is a function of ion energy *f*(E). The integral can therefore be solved by using Simpson's rule [39]:

$$\int_{Ef}^{Ei} f(E)dE = \frac{E_i - E_f}{6} \times \left[f(E_i) + f\left(E_f\right) + 4f\left(\frac{E_i + E_f}{2}\right)\right] \tag{3.25}$$

The energy loss correction factor is therefore described by equation 3.25:

$$F(\Delta E) = \frac{1}{\Delta x \times \sigma_i} \times \left[\frac{E_i - E_f}{6} \times \left[\frac{\sigma_i(E_i)}{S(E_i)} + \frac{\sigma_i(E_f)}{S(E_f)} + 4\left[\frac{\sigma_i(^{E_f + E_i}/_2)}{S(^{E_f + E_i}/_2)} \right] \right] \right] \tag{3.26}$$

Exit Energy

For evaluation of F(E), the exit energy is determined through equation (3.19):

$$\Delta x = \int_{Ef}^{Ei} \frac{1}{S(E)} dE \tag{3.19}$$

This requires that the thickness of the target be known accurately, hence the RBS characterization described in chapter 4.

From equation 3.19, a polynomial fit can be made for the inverse of stopping powers 1/S (from the SRIM database) against ion energies E for an estimated energy interval (E_i-E_f). Based on this, the inverse of total stopping powers is a function of energy described by:

$$h(E) = \frac{1}{S(E)} \tag{3.27}$$

Thus the target thickness is given by:

$$\Delta x = \int_{Ef}^{Ei} h(E)dE = g(E_i) - g(E_f) \tag{3.28}$$

where g(E) is the integral of the function h(E). This can be re-arranged so that:

$$g(E_i) - \Delta x = C = g(E_f) \tag{3.29}$$

As the thickness of the target and the function $g(E_i)$ at the known incident energy E_i are well defined, the algebraic expression on the left-hand side does not change and hence is a constant 'C'. From this arrangement one can write:

$$C - g(E_f) = 0 \tag{3.30}$$

To solve for E_f, a function Y(E) is defined;

$$Y(E) = C - g(E) \tag{3.31}$$

where $Y(E_f)=0$.

The exit energy E_f is then obtained from a plot of Y(E) vs E, i.e. the energy axis intercept is equal to E_f. Figure 3.15 shows an illustrative plot of Y(E) against ion energy to determine the ion exit energy:

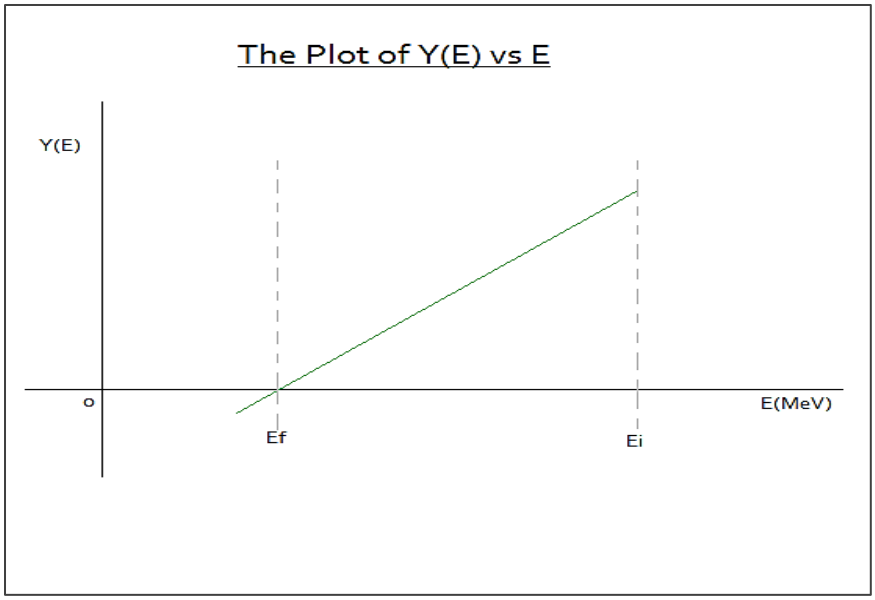

Figure 3.15. *Exit energy plot illustration.*

For the target samples used in this work (see chapter 4), the proton energy loss was less than 2%, to an extent that the energy loss correction factor for protons $F_p(E)$ was practically equal to one. For the heavier ions, ^{12}C and ^{35}Cl, the correction had to be made. And so the assumption made in equation 3.9 was considered not to be valid. Therefore the final equation used for the evaluation of heavy ion induced X-ray production cross sections was, from equation 3.12:

$$\sigma_X(HI) = \frac{N_X(HI)}{N_X(p)} \times n_f(HI) \times \frac{\varepsilon_p}{\varepsilon_{HI}} \times F_{HI}(\Delta E) \times \sigma_X(p) \tag{3.32}$$

where the ratio $\frac{\varepsilon_p}{\varepsilon_{HI}}$ corrects for changes in the X-ray detection efficiency due MI effects.

Chapter 4
Experimental results and discussion

4.1 Introduction

In this chapter, the experimental results obtained are presented and discussed. The results include thickness determination of the target samples used and also report on the calculations of the X-ray production cross sections in oxides of V, Zr and Sn due to protons, carbon and chlorine MeV ion beams. X-ray production cross section results are discussed in comparison to theoretical PWBA and ECPSSR approximations.

4.2 Target samples and thickness determination

4.2.1 Target material samples

The target samples used for Heavy ion induced X-ray production cross section measurements were Vanadium, Zirconium and Tin metal oxide films deposited separately on Mylar (Polyethylene terephthalate) using electron beam thin film vapor deposition. Samples were purchased from Sigma-Aldrich in the form of 1cm diameter discs mounted on ring shaped Perspex frames. This section presents measurement of the thickness of the thin film oxides used, for the purpose of determining the energy loss correction factors for heavy ion induced X-ray production cross sections as described in chapter 3. SIMNRA by Dr.Matej Mayer from the *Max-Planck-Institut für Plasmaphysik, Germany* was used to analyze RBS data for the determination of target material thicknesses [14].

4.2.2 RBS thickness measurement

2MeV He^{+} ion beams were used to conduct Rutherford Backscattering Spectroscopy (RBS) measurements on the selected metal oxide samples. These measurements were done on the

scanning nuclear microprobe at iThemba LABS (TAMS) under high vacuum conditions (10^{-6} torr). The backscattered He^{+} ions were counted using a surface barrier Canberra PIPS detector positioned at an angle of 150^{o} from the 0^{o} incident beam angle, for a counting period of about 30 minutes in order to attain reliable statistics.

Energy calibration

The default spectra of SIMNRA describes counts versus channel numbers. In order to calibrate the spectra in terms of the number of backscattered particles verses energy, samples of known elements with known elemental energy peaks were used. From these, the channel numbers of the respective element peaks from the individual sample spectrums where recorded. Samples of V, Zr and Sn oxide films on Mylar, as well as TaN on Si were used. Table 4.1 shows the surface energy, calculated by SIMNRA [14], for each element in the calibration sample and the corresponding peak channel number.

Table 4.1 *Energy calibration table of values.*

Element	Channel number (#)	Surface Energy (KeV)
V	332	1490.74
Zr	343	1697.72
Sn	346	1763.43
Ta	350	1841.50

A plot of ion backscattering energy (obtained from SIMNRA kinematic calculations) against corresponding peak channel numbers gives a straight line fit that is used to define the calibration

parameters for the SIMNRA spectra. Figure 4.1 shows the calibration plot for 2.0 MeV He^+ ions in V, Zr, Sn and Ta:

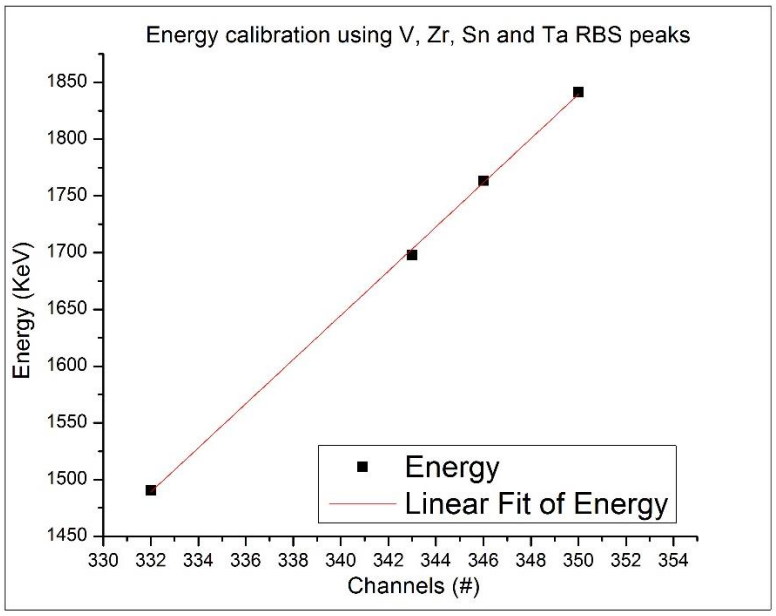

Figure 4.1 *Energy per channel Calibration plot using Origin 8 pro.*

The calibration plot in figure 4.1 shows a linear relationship between energy and channels. For the data shown here, the energy calibration parameters are;

Slope (energy per channel) = 5.63 KeV/ch and intercept (energy offset) = - 18.9 KeV

From this, the calibration of the SIMNRA spectra is established using the slope of the graph as the energy per channel and the intercept, which describes the calibration offset (in KeV). These parameters are then used in the simulation of an experimental RBS spectrum for different sequential runs under the same experimental condition.

4.2.3. RBS spectra analysis

This section describes data analysis for thickness evaluation of the various thin films along with their stoichiometry. Figure 4.2 shows simulated and experimental calibrated spectra for 2.0 MeV He^+ on the vanadium oxide sample:

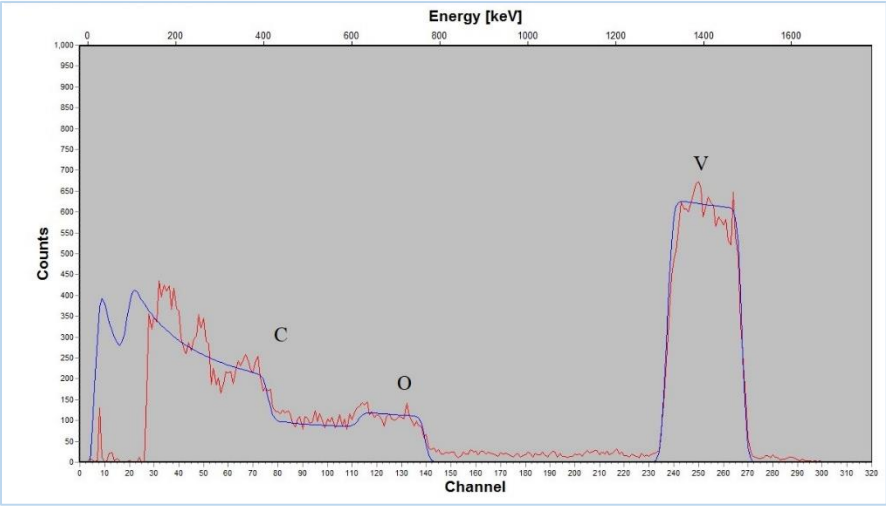

Figure 4.2 *Simulated and experimental RBS spectra for 2.0 MeV He^+ in Vanadium oxide.*

Where the peak on the far right represents helium ions backscattered from vanadium atoms in the metallic oxide layer. The peaks on the left describe the backscattered helium ions due to oxygen atoms in the oxide layer and the mylar, and carbon atoms from the Mylar ($C_8H_{10}O_4$) substrate. It should be pointed out that there is no peak corresponding to hydrogen atoms because the kinematics of the $^4He^+$-^1H atom collision forbid $^4He^+$ to backscatter from ^1H. In the simulation therefore, the hydrogen content in mylar is assumed to be the natural stoichiometric amount.

The simulated fit does not perfectly match the experimental fit due to inherent limitations in experimental conditions such as the poor resolution of the detector, and relative energy spread of the incident ion beam. Other limitations may include straggling and stopping force inaccuracies. The spectrum fitted however is fairly accurate in approximating the experimental spectrum and therefore the fit parameters can be used to determine the thickness of the target film. The thickness

of the sample in SIMNRA is given in areal units of atoms/cm^2. Table (4.1.) gives the thickness and average stochiometry for all the three films measured.

Figures 4.3 and 4.4 show RBS spectra for Zr and Sn due to 2 MeV He^+ ion beams;

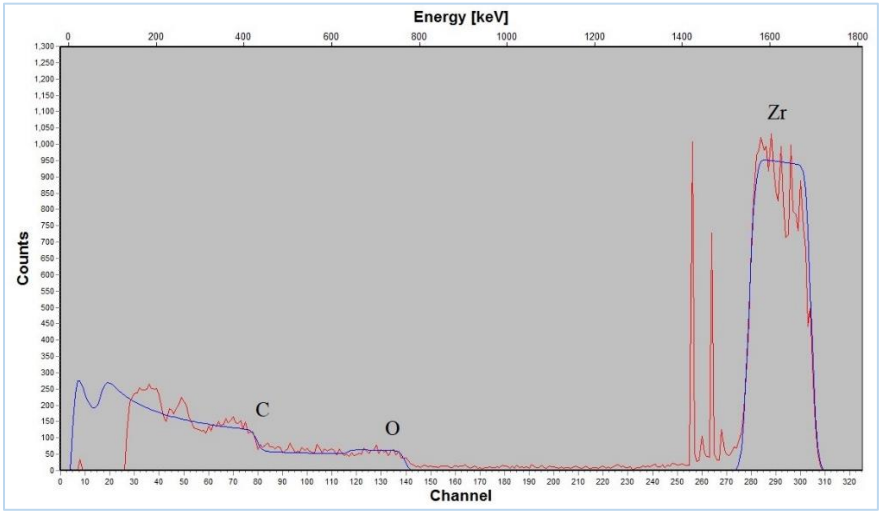

Figure 4.3 *Simulated and experimental RBS spectra for 2.0 MeV He^+ in Zirconium oxide.*

It should be pointed out that the spikes on the left hand side of the zirconium peak are experimental artifacts which may have occurred during data acquisition. These however do not affect, in any way, the accuracy of the results obtained from this spectra which are therefore considered valid.

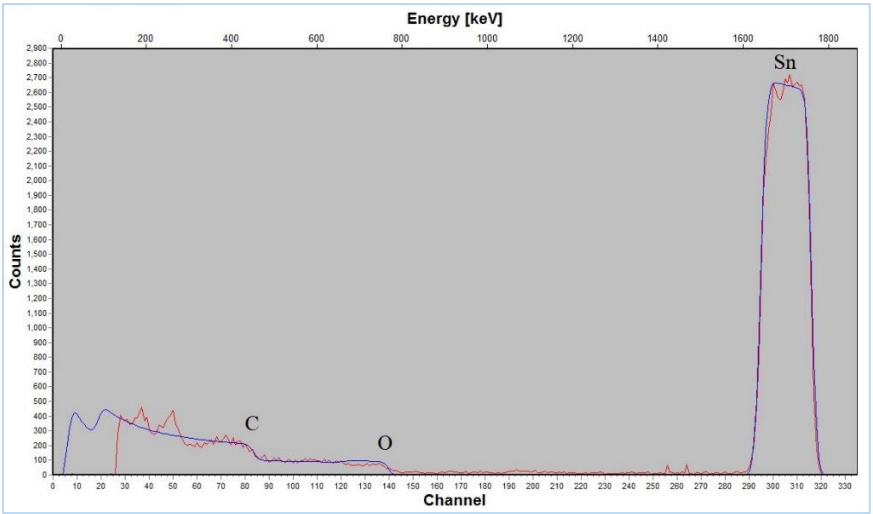

Figure 4.4 *Simulated and experimental RBS spectra for 2.0 MeV He^+ in Tin oxide.*

Table 4.2. *Target thin film thickess in atoms/cm^2 obtained from SIMNRA.*

Thin Film	n	Δx (1e15 atoms/cm^2)
Vanadium oxide (V_nO_{1-n})	0.40	1638
Zircornium oxide (Zr_nO_{1-n})	0.43	1180
Tin oxide (Sn_nO_{1-n})	0.49	915

4.1.3 Thickness uncertainty

The main contributors to uncertainty in the measurement of film thickness using RBS are stopping force of He ions in the films at 3.1% [14]; RBS detector resolution (ΔE) ≈1%, SIMNRA code accuracy 0.83% [14], and layer thickness inhomogeneity estimated at ≈1% (ΔT).

The combined uncertainty estimate for the measured layer thickness is then given by;

$$\Delta X(\%) = \pm\sqrt{(\Delta S)^2 + (\Delta E)^2 + (\Delta C)^2 + (\Delta T)^2} = 3.5\% \qquad (4.1)$$

The thickness of thin films inclusive of uncertainty to measurement is given by the table below:

Table 4.3. *Target thin film thickness inclusive of uncertainty in atoms/cm^2.*

Thin film	n	Δx (1e15 atoms/cm^2)
V_nO_{1-n}	0.4	1638 ± 57
Zr_nO_{1-n}	0.43	1180 ± 41
Sn_nO_{1-n}	0.49	915 ± 32

4.2. X-ray peak analysis

The data acquisition system, OMDAQ, was used to sort signals from detected X-rays according to the amplitude of generated voltage pulses, which in turn depends on the energy of the X-ray. The same was done for backscattered ions. The acquired X-ray yields and backscattered ions were then determined using the peak integration function of OMDAQ which incorporates background subtraction under each peak.

4.3. X-ray production cross section evaluation

X-ray yields were acquired from the scanning nuclear microprobe for proton, helium, carbon and chlorine based ion-atom collisions. These were conducted at ion energies of 0.1-1.0 MeV/u. For the purpose of investigating the effect of ion mass on the X-ray production cross section, an exploratory evaluation of X-ray yields due to proton and carbon ion beams at 1.0 MeV/u and 2.0 MeV/u respectively was conducted. These are shown in the following figure:

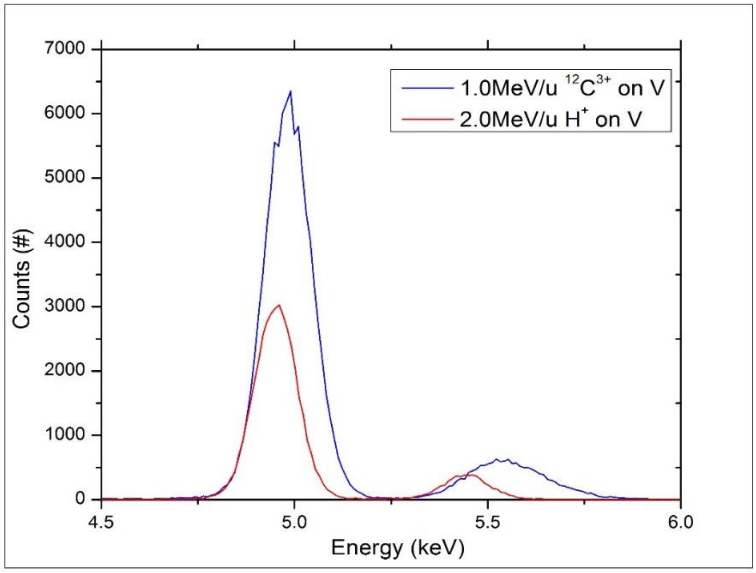

Figure 4.5 *H^{+} and $^{12}C^{3+}$ ion induced K-shell X-ray yields in Vanadium at 1.0 and 2.0 MeV/u ion energies.*

From figure 4.5, the incident projectile is seen to have an effect of increasing the X-ray production cross section as the mass of the projectile increases. This is seen to be the case even though the energy per unit mass (or the velocity) of the ^{12}C ions is much less than that of protons. This is possibly due to a larger electronic screening effect of the target atom on the incident carbon projectiles. This effect may thus result in radiative multiple ionization events as the electron cloud of the incident ion interacts with that of the target atom, hence causing increase in the fluorescence yield and subsequent number of X-ray photons. This phenomena was also observed by Msimanga *et.al* [3] for silicon ion beams on Tantalum. The influence of ion mass and velocity on X-ray yield is also observed in Figure 4.6 [3]:

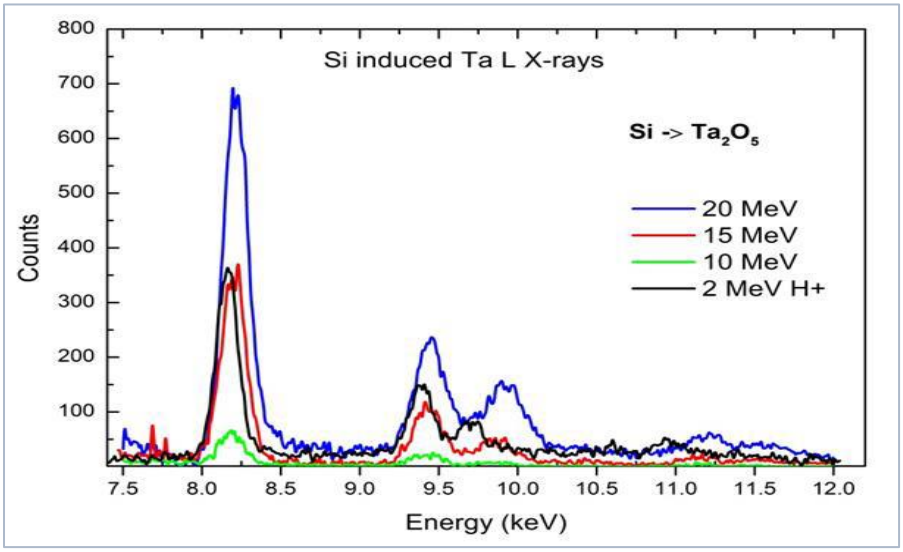

Figure 4.6 *2.0 MeV H^+ and 10 – 20 MeV Si induced L-shell X-ray yields in Ta. [3]*

For a specific projectile ion, the effect of energy on the X-ray yields is exemplified in the following figure:

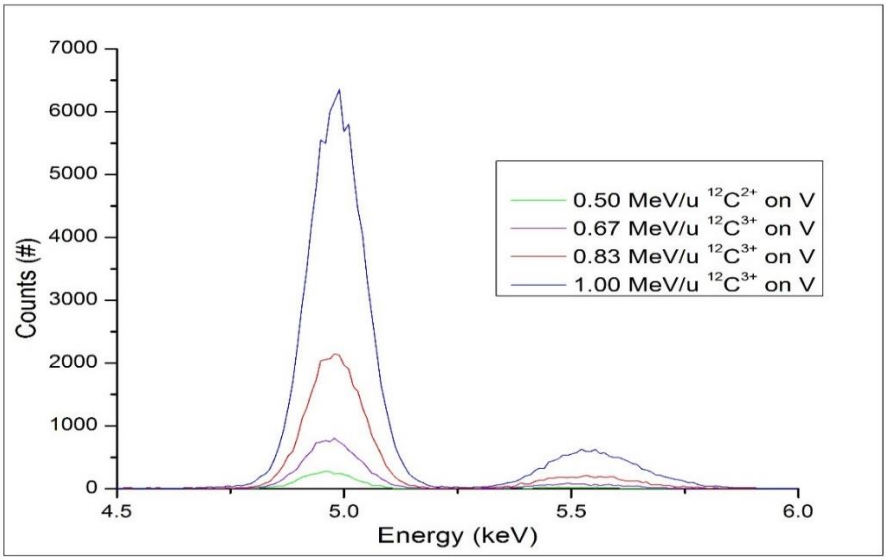

Figure 4.7 *$^{12}C^{2+}$ and $^{12}C^{3+}$ ion induced K-shell X-ray yields in V at 6 - 12MeV ion energies.*

Figure 4.7 shows a clear substantial increase in the X-ray yield due to carbon ions as the velocity of the ions increases. This implies a higher ionization cross section. This may be due to an increasing probability of ion interaction with the electron cloud of the target atom. The data gathered in figures (4.5), (4.6) and observations made in (4.7) suggests that as the velocity of the incident ions increases so does the probability of ion interaction with the target electrons that results in direct ionizations. An increasing velocity also leads to increasing radiative electron capture probabilities which result in the production of X-ray photons.

The X-ray production cross sections are evaluated in terms of the number of incident ions which are measured through the observation of the number of X-ray photons and backscattered counts (chapter 3, 3.6). This is given by Equation (3.8) which evaluates the proton induced X-ray production cross section as follows:

$$\sigma_x = \frac{N_X}{N_B} \times \frac{A \times \Delta\Omega}{N_A \times \varepsilon \times \beta} \times \sigma_B \quad (3.8)$$

As the values of the experimental parameters remain the same for each ion-target atom combination, the following ratio of parameters may be considered to be a constant, K, as described in equation 3.9 in chapter 3.

$$K = \frac{A \times \Delta\Omega}{N_A \times \varepsilon \times \beta} = \frac{N_B}{N_X} \times \frac{\sigma_X}{\sigma_B} \quad (3.9)$$

The following table gives the K-factors for V, Zr and Sn due to 2MeV proton beams:

Table 4.4. *Target element(s) proton induced K-factor(s).*

Target Element	K-factor
V	57.6
Zr	136.6
Sn	84.2

These K-Factors where determined using the following values described table 4.5:

Table 4.5 *Experimental and physical parameters used for the determination of proton based K-factors.*

Target elements	N_{Xp}	N_{Bp}	$\sigma_{Xp\ (b)}$	$\sigma_{Bp\ (mb)}$
V	132833	9313	161.498	196.41
Zr	161594	10390	1259.87	593.28
Sn	137545	20920	512.532	925.99

The proton induced X-ray production cross section $\sigma_x(p)$ was obtained from the ERCS08 code [28], and the proton backscattering cross section $\sigma_B(p)$ was obtained from calculations by the SIMNRA code [14].

4.3.1. Carbon induced X-ray production cross section evaluation

From the constituent physical parameters of the respective K-factors, the heavy ion induced X-ray production cross section can be determined. This incorporates the incident ion correction factor as described in chapter 3 (section 3.6) and thus the carbon ion induced X-ray production cross section, is according to equation (3.10) in chapter 3, given by:

$$\sigma_x(C) = K \times \frac{N_x(C)}{N_B(C)} \times \sigma_B(C) \tag{4.2}$$

The carbon induced X-ray production cross sections measured under the same experimental conditions as the proton beam measurements, for Vanadium (V), Zirconium (Zr) and Tin (Sn) are then described by equations (4.3), (4.4) and (4.5) respectively:

$$\sigma_x(C,V) = (57.6) \times \frac{N_x(C,V)}{N_B(C,V)} \times \sigma_B(C,V) \tag{4.3}$$

$$\sigma_x(C,Zr) = (136.6) \times \frac{N_x(C,Zr)}{N_B(C,Zr)} \times \sigma_B(C,Zr) \tag{4.4}$$

$$\sigma_x(C,Sn) = (84.2) \times \frac{N_x(C,Sn)}{N_B(C,Sn)} \times \sigma_B(C,Sn) \tag{4.5}$$

By applying these equations for the various ion-atom combinations, varying incident ion energies and K factors, the following results were obtained:

Carbon in Vanadium: K = 57.4

Table 4.6 *4 – 12 MeV Carbon induced K-shell X-ray production cross sections in Vanadium.*

Energy (MeV)	**N_X(C)**	**N_B(C)**	**σ_B (mb)**	**σ_X (C, V) (b)**
4.00	1025.00	36730.00	1592.00	2.53
6.00	3619.00	8077.00	709.47	18.07
8.00	12154.00	4246.00	399.55	65.05
10.00	33703.00	3407.00	255.89	143.98
12.00	94190.00	2527.00	177.78	377.52

Carbon in Zirconium: K = 136.6

Table 4.7 *4 – 12 MeV Carbon induced L-shell X-ray production cross sections in Zirconium.*

Energy (MeV)	**N_X(C)**	**N_B(C)**	**σ_B (mb)**	**Experimental σx (C, Zr) (b)**
4.00	196671.00	139357.00	5132.90	1009.85
6.00	174224.00	16158.00	2291.00	3413.40
8.00	240575.00	6158.00	1291.40	6974.98
10.00	624706.00	5426.00	827.57	13176.94
12.00	341422.00	1536.00	575.19	17693.83

Carbon on Tin: K = 84.2

Table 4.8 *4 – 12 MeV Carbon induced L-shell X-ray production cross sections in Tin.*

Energy (MeV)	N_X (C)	N_B (C)	σ_B (mb)	σ_X (C, Sn) (b)
4.00	28659.00	104360.00	8091.20	185.57
6.00	60750.00	37212.00	3615.90	492.26
8.00	81402.00	12835.00	2039.50	1081.26
10.00	190619.00	9615.00	1307.40	2165.24
12.00	259779.00	4963.00	908.94	3979.29

4.3.2. Chlorine induced X-ray production cross sectional evaluation

Chlorine ion beam induced X-ray production cross sections in Zr and Sn were evaluated using equation (3.10) from chapter 3:

$$\sigma_x(Cl) = K \times \frac{N_x(Cl)}{N_B(Cl)} \times \sigma_B(Cl) \tag{4.6}$$

Similarly, the Chlorine induced X-ray production cross sections measured under the same experimental conditions as the proton beam measurements for Zirconium (Zr) and Tin (Sn) are described by equations (4.7) and (4.8) respectively:

$$\sigma_x(Cl, Zr) = (136.6) \times \frac{N_x(Cl, Zr)}{N_B(Cl, Zr)} \times \sigma_B(Cl, Zr) \tag{4.7}$$

$$\sigma_x(Cl, Sn) = (84.2) \times \frac{N_x(Cl, Sn)}{N_B(Cl, Sn)} \times \sigma_B(Cl, Sn) \tag{4.8}$$

The physical parameters used for cross section evaluation of the different chlorine-atom interactions are given in the following table:

H^+ on Zr

Table 4.9 *Proton induced X-ray photon and ion backscattering counts.*

Energy (MeV)	**N_X (p)**	**N_B (p)**	**σ_X (p) (b)**	**σ_B (p) (mb)**	**K-factor**
2.00	164927.00	10890.00	1259.87	593.28	136.60

Cl on Zr: K = 136.6

Table 4.10 *7 – 35 MeV Chlorine induced X-ray production cross sections in Zirconium.*

Energy (MeV)	**N_X(Cl)**	**N_B(Cl)**	**σ_B(Cl) (mb)**	**σ_x (Cl, Zr) (b)**
7.00	95991.00	10619.00	10334.71	13099.28
14.00	968966.00	11726.00	2619.77	30354.56
21.00	59895.00	247.00	1169.76	39773.38
28.00	65985.00	103.00	659.52	59243.15
35.00	104349.00	87.00	422.68	71085.80

H^+ on Sn

Table 4.11 *Proton induced Sn X-ray photon and backscattering counts*

Energy	N_X (p)	N_B (p)	σ_X(p) (b)	σ_B (p) (mb)	K-factor
2	165236	28253	512.532	925.99	84.2

Cl on Sn

Table 4.12 *7 – 35 MeV Chlorine induced L-shell X-ray production cross sections in Tin.*

Energy	N_X (Cl)	N_B (Cl)	σ_B (Cl) (mb)	σ_X (Cl, Zr) (b)
7.00	99024.00	46102.00	18098.15	3679.00
14.00	390370.00	14763.00	4602.13	11516.89
21.00	74253	793.00	2057.08	18229.16
28.00	67961.00	299.00	1160.41	24961.73
35.00	64043.00	136.00	743.94	33154.71

4.4. Corrections to experimental cross sections

4.4.1 X-ray detection efficiency correction factor (F_ε)

As mentioned in chapter 2, the detection efficiency describes the extent to which an X-ray detector detects X-ray photons [21]. This parameter ε_x can be determined using equation 4.12, derived from equations 3.5 and 3.7 of chapter 3 as described below;

$$N_X = \sigma_X \times \frac{N_i \times N_A \times \varepsilon_x \times \beta \times \Delta x'}{A \times F(E)} \qquad (3.5)$$

$$N_i = \frac{N_B \times \cos\alpha}{\sigma_B \times \Delta x \times \Delta\Omega} \tag{3.7}$$

It should be noted that the target thickness (Δx) in equation 3.5 is not of the same units (g/cm^2) as that in equation 3.7 (Atoms/cm^2). The thicknesses do not therefore simply cancel each other out. To convert both thicknesses to the same unit (cm), the thickness in 3.5 and 3.7 should be divided by the atomic and mass densities respectively. This can be expressed as;

$$\frac{\Delta x}{\rho_{Atm}} = \frac{\Delta x'}{\rho_m} = cm \tag{4.9}$$

In essence;

$$\frac{\Delta x}{\Delta x'} = \frac{\rho_{Atm}}{\rho_m} \tag{4.10}$$

Thus;

$$\frac{\Delta x}{\rho_{Atm}} \times \frac{\rho_m}{\Delta x'} = 1 \tag{4.11}$$

Therefore;

$$\varepsilon_x = \frac{N_{Xp}}{N_{Bp}} \times \frac{\sigma_{Bp}}{\sigma_{Xp}} \times \frac{A}{N_A} \times \frac{\Delta\Omega_B}{\beta} \times \frac{\rho_{Atm}}{\rho_m} \tag{4.12}$$

Where ρ_{Atm} and ρ_m are obtained from the SRIM database (see Appendix A).

Due to the observed clear X-ray characteristic energy shift that occurs due to an increasing projectile mass (as observed in figures (4.5) and (4.6)), the detection efficiency of X-ray photons at new heavy ion induced characteristic energies cannot be assumed to be the same as that of known X-ray characteristic energies due to proton ion beams. In order to compensate for the change in detection efficiencies, an evaluation of the variation of detection efficiency against characteristic energies has to be made.

Table 4.13 *Table of proton induced X-ray detection efficiencies.*

X-ray line	E(KeV)	$N_x(p)$	$N_B(p)$	$\sigma_B(p)$ (mb)	$\sigma_X(p)$ (b)	ε_{xp}
V-Kα	4.95	13283.00	9313.00	196.41	161.50	0.00132
Zr-Lα	2.04	161594.00	10390.00	593.28	1259.87	0.00061
Sn-Lα	3.44	137545.00	20920.00	925.99	512.53	0.00087

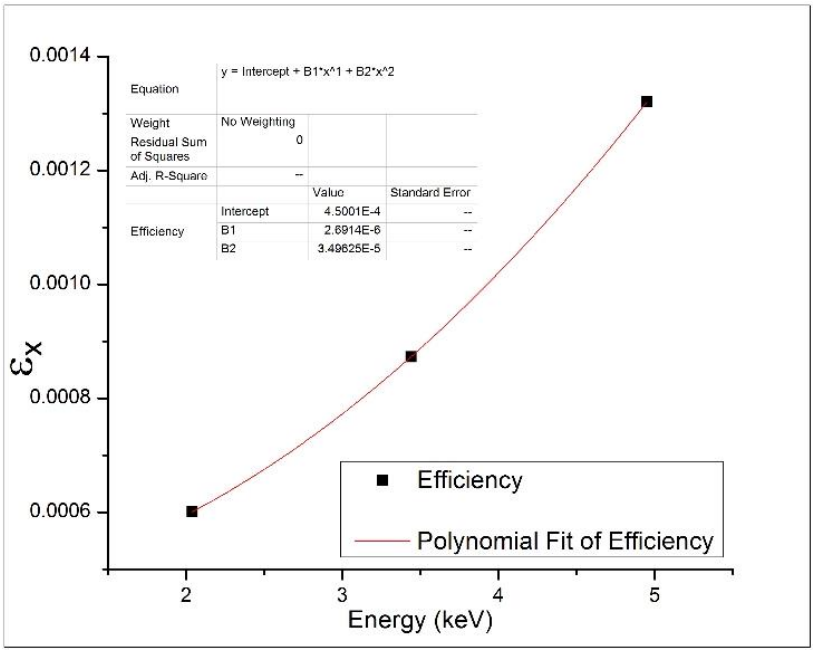

Figure 4.8. *Detection efficiencies for V, Zr, and Sn due to 2MeV H^+ ion beams.*

The polynomial trend equation was used for the determination of detection efficiencies at heavy ion characteristic X-ray energies:

$$\varepsilon = (3.49625 \times 10^{-5})E^2 + (2.6914 \times 10^{-6})E + (4.5001 \times 10^{-4}) \qquad (4.13)$$

Carbon and chlorine induced X-ray detection efficiencies were calculated and are given in tables 4.14 and 4.15 below:

Table 4.14 *Carbon induced X-ray detection efficiencies.*

X-ray line	**$^{12}C^{q+}$ induced X-ray energy**	**ε_{Xp}**	**ε_{XC}**	**$F_{\varepsilon}(C)$ ($\varepsilon_{Xp}/\varepsilon_{XC}$)**
V-Kα	5.2665	0.00132	0.00143	0.949
Zr-Lα	2.0610	0.00061	0.000604	1.030
Sn-Lα	3.5665	0.00084	0.000904	0.965

Table 4.15 *Chlorine induced X-ray detection efficiencies.*

X-ray line	**$^{35}Cl^{q+}$ induced X-ray energy**	**ε_{Xp}**	**ε_{XCl}**	**$F_{\varepsilon}(Cl)$ ($\varepsilon_{Xp}/\varepsilon_{XCl}$)**
Zr-Lα	2.080	0.000610	0.000607	1.020
Sn-Lα	3.578	0.000840	0.000907	0.962

4.4.2 Energy loss correction factor ($F_{\Delta E}$)

The variation of ion energies as the projectile ions penetrates a certain thickness in the material sample implies a changing X-ray production cross section (as it is energy dependent). In order to correct for the effects of ion energy loss on the X-ray production cross section, the following energy loss correction factor is implemented for all ion-atom combinations reported herein [39]:

$$F_{\Delta E} = \frac{1}{\Delta x \times \sigma_i} \times \left[\frac{E_i - E_f}{6} \times \left[\frac{\sigma_i(Ei)}{S(E)_{Ei}} + \frac{\sigma_i(Ef)}{S(E)_{Ef}} + 4 \left[\frac{\sigma_i({}^{Ef+Ei}/_{2})}{S(E)_{({}^{Ef+Ei}/_{2})}} \right] \right] \right] \quad (3.26)$$

As this correction factor is dependent on energy, the final exit energy of the incident ion is determined using the following function (see chapter 3, section 3.6.2.1):

$$Y(E) = C - G(E) \quad (3.31)$$

Tables of Y(E) for various heavy ion-atom combinations with their respective incident energies are given in appendix B. These values were fitted against the respective variable energy values that describe the integral of the inverse stopping power g(E). As the exit energy is obtained at the X-intercept of the fit (Y(E) =0), logarithmic fits were made for each plot attained where trend equations were then used to determine the exit energy. This was done by solving for the value of E of the trend equations at the point Y(E) = 0, calculated using Mathcad 5. An example of this is illustrated by the energy loss analysis of 4 MeV carbon ions in Vanadium. The obtained Y(E) values are given by table (4.16):

Table 4.16. *Energy loss analysis for 4 MeV carbon in Vanadium for exit energy determination.*

Energy	Y(E)
5	-0.00065
4	2.16E-05
3	-0.00499
2	-0.02625
1	-0.11155

The exit energy plot for C in V is given by:

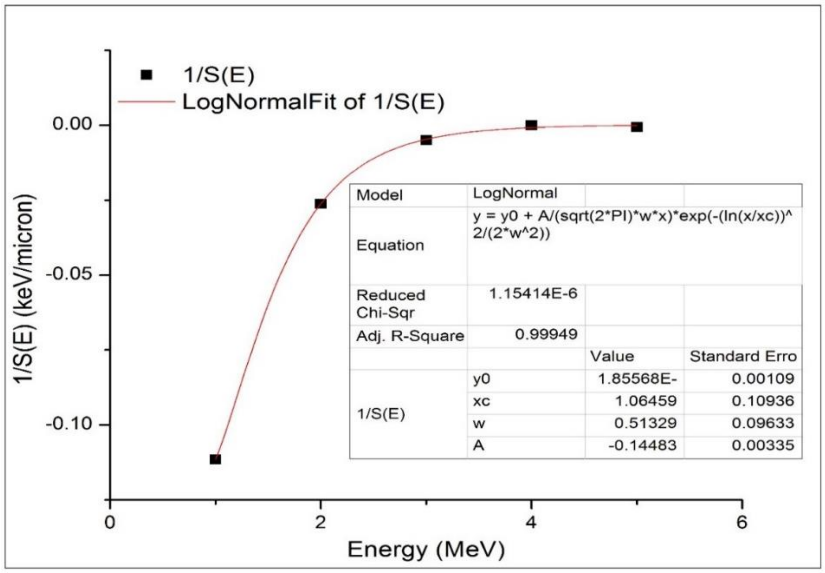

Figure 4.9. *Inverse stopping powers versus ion energy*

From this, the exit energy can easily be calculated using the logarithmic trend-line equation. The intercept of the energy axis of the plot is the exit energy (at Y(E) = 0), therefore solving for *E* at Y(E) = 0 gives the exit energy. Tables of the inverse-stopping powers against respective energies for the determination of ion exit energies are given in Appendix B. From these, the exit energies are given in appendix C of this dissertation.

A plot of S(E) (electronic and nuclear stopping powers) vs ion Energies was made, where S(E) values were obtained from SRIM. A 5 order polynomial fit was conducted in order to better model the observed data trend. The polynomial trend equations were then used to determine stopping powers at exit energies, for input into the energy loss correction factor.

While a much more economical way of determining stopping powers at exit energies would be to use SRIM, this was not possible due to the software's inherent inability of producing stopping powers at exact energy inputs. SRIM Stopping powers where produced at rounded energy values, which in some cases saw the corresponding energy values being far off the mark from the actual

exit energies. The code in this case was seen to be unreliable. The calculated polynomial equations therefore were used to approximate SRIM stopping powers, where exact exit energy values could be inputted in order to produce correlating stopping powers.

These equations were computed using Mathcad 5 where the functions are the stopping powers and the values of x are the energy inputs. Figure 4.10 shows a Graphical User Interface of Mathcad 5:

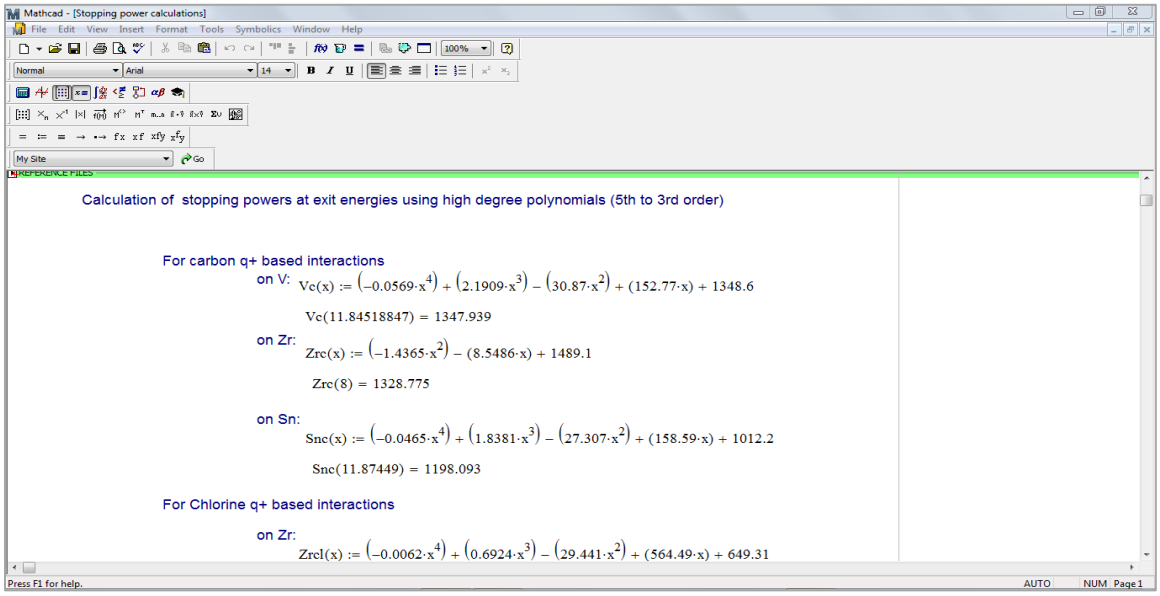

Figure 4.10. *Graphical User Interface of Mathcad 5 used for the calculation of stopping powers at exit energies.*

The polynomial trend equations used for the determination of stopping powers at exit energies for $^{12}C^{q+}$ in V (4.14), Zr (4.15), Sn (4.16) and $^{35}Cl^{q+}$ in Zr (4.17) and Sn (4.18) are as follows:

$$V\_C(x) := (-0.0569 \cdot x^4) + (2.1909 \cdot x^3) - (30.87 \cdot x^2) + (152.77 \cdot x) + 1348.6 \tag{4.14}$$

$$Zr\_C(x) := (-1.4365 \cdot x^2) - (8.5486 \cdot x) + 1489.1 \tag{4.15}$$

$$Sn\_C(x) := (-0.0465 \cdot x^4) + (1.8381 \cdot x^3) - (27.307 \cdot x^2) + (158.59 \cdot x) + 1012.2 \tag{4.16}$$

$$\mathrm{Zr\_Cl}(x) := \left(-0.0062 \cdot x^4\right) + \left(0.6924 \cdot x^3\right) - \left(29.441 \cdot x^2\right) + (564.49 \cdot x) + 649.31 \tag{4.17}$$

$$\mathrm{Sn\_Cl}(x) := \left(0.1223 \cdot x^3\right) - \left(10.807 \cdot x^2\right) + (325.55 \cdot x) + 1342.3 \tag{4.18}$$

4.5. Corrected Heavy ion induced X-ray production cross section

Heavy ion induced X-ray production cross sections with effected correction factors are given by:

$$\sigma_x(Cl) = K \times \frac{N_x(HI)}{N_B(HI)} \times \sigma_B(HI) \times F_{\varepsilon x} \times F_{\Delta E} \tag{4.19}$$

4.5.1. Carbon-ions energy loss corrections

Table (4.17) describes carbon ion beams' exit energies at 4 - 12 MeV due to V, Zr and Sn metal oxide films:

C^{q+} Exit Energies

Table 4.17 *Table of 4 – 12 MeV Carbon ion exit energies.*

Energy (MeV)	V	Zr	Sn
4.00	3.63	3.66	3.73
6.00	5.64	5.67	5.72
8.00	7.66	7.69	7.73
10.00	9.67	9.71	9.74
12.00	11.69	11.72	11.74

Table (4.18) describes energy loss percentages for carbon ion beams at 4-12 MeV due to V, Zr and Sn metal oxide thin films

Table 4.18. *Carbon ion energy loss percentages in V, Zr and Sn at 4 – 12 MeV.*

Energy (MeV)	V	Zr	Sn
4.0	9.2%	8.3%	6.9%
6.0	6.0%	5.5%	4.6%
8.0	4.3%	3.9%	3.4%
10.0	3.3%	2.9%	2.6%
12.0	2.6%	2.3%	2.1%

Figure 4.11 describes carbon ion beam energy loss in V, Zr and Sn due to target element nuclear and electronic stopping powers.

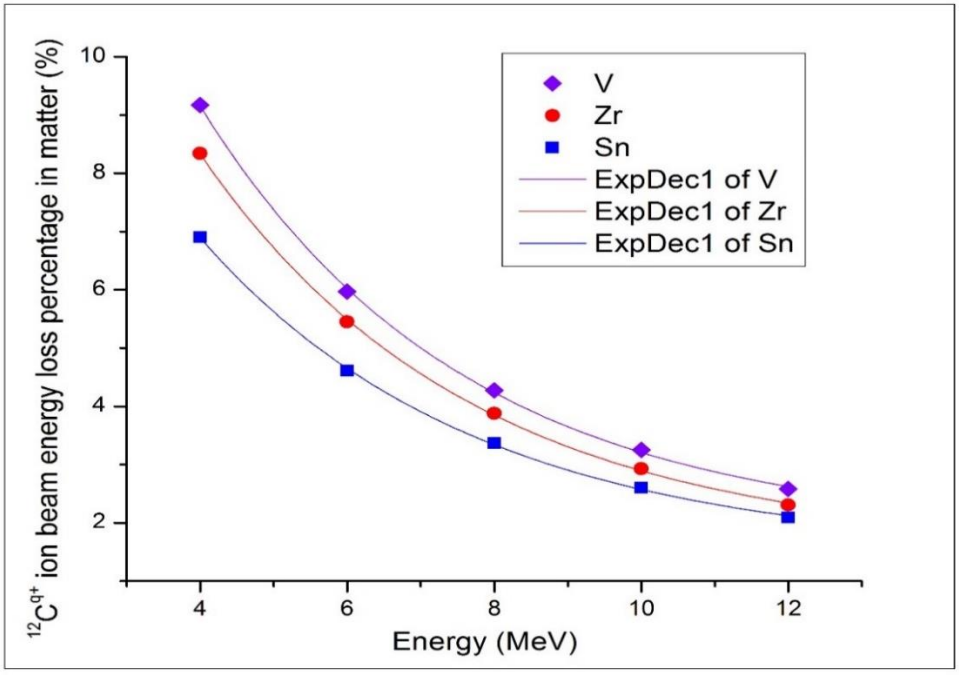

Figure 4.11. *Carbon ion beam energy loss percentage in V, Zr and Sn.*

Theoretical cross sections are used in equation 3.26 (for σ(E)) for all carbon-atom combinations and are calculated from fits to the ECPSSR theory, obtained using the ERCS08 code [28]. This is because, for a narrow energy range (such as E_i - E_f), theoretical data deviates from experiment by a constant factor but the energy dependency (or trend) is the same. This constant factor cancels out in equation 3.26. So the use of the ECPSSR based fit is justified. Table (4.19) describes energy loss correction factors for V, Zr and Sn due to 4-12MeV C^{q+} ion beams:

C^{q+} Energy loss correction factors ($F_{\Delta E}$)

Table 4.19. *Energy loss correction factors for carbon induced X-ray production cross sections in V, Zr and Sn.*

Energy (MeV)	V	Zr	Sn
4.00	0.77	0.88	0.89
6.00	0.88	0.92	0.94
8.00	0.91	0.94	0.95
10.00	0.93	0.96	0.96
12.00	0.95	0.97	0.97

4.5.1.1 Carbon Projectiles

The corrected X-ray production cross sections for 4-12MeV $^{12}C^{q+}$ in V, Zr and Sn are given in the following tables, compared with PWBA and ECPSSR predictions:

$^{12}C^{q+}$ in V

Table 4.20. *Experimental X-ray production cross sections in V due to 4-12 MeV Carbon ion beams. (Corrected)*

Energy (MeV)	σ_X(raw)	σ_X(corrected)	PWBA (b)	ECPSSR (b)
4.00	2.53	1.94	99.65	4.29
6.00	18.07	15.85	327.56	26.10
8.00	65.05	59.24	702.76	90.20
10.00	143.98	134.54	1207.95	226.18
12.00	377.52	358.64	1816.18	459.99

$^{12}C^{q+}$ in Zr

Table 4.21. *Experimental X-ray production cross sections in Zr due to 4-12 MeV Carbon ion beams. (Corrected)*

Energy (MeV)	σ_X(raw)	σ_X(corrected)	PWBA(b)	ECPSSR (b)
4.00	1009.85	910.16	3580.46	565.99
6.00	3413.40	3220.33	7876.43	1956.30
8.00	6974.98	6713.61	12934.52	4449.98
10.00	13176.94	12842.51	18169.76	7892.68
12.00	17693.83	17576.24	23248.24	11994.02

$^{12}C^{q+}$ in Sn

Table 4.22. *Experimental X-ray production cross sections in Sn due to 4-12 MeV Carbon ion beams.*

Energy (MeV)	σ_X(raw)	σ_X(corrected)	PWBA (b)	ECPSSR (b)
4.00	185.57	165.20	545.74	115.94
6.00	492.26	463.35	1773.73	373.83
8.00	1081.26	1032.04	3260.15	855.91
10.00	2165.24	2092.01	5079.79	1638.91
12.00	3979.29	3883.14	7135.34	2697.92

Ionization cross sections of the classical, modified PWBA and basic ECPSSR theory and the electron capture corrected ECPSSR theory were obtained from an ERCS08 code. These cross sections were converted to the X-ray production cross section using known fluorescence yields suggested by Campbell et.al [20]. The total K- and L-shell Ionization cross sections obtained from the ECRS08 code where converted to X-ray production cross sections using the following equation where σ_i^X, σ_i^I and ω_K are the total X-ray production cross sections at the I shell, the total ionization cross section at the I shell and the total fluorescence yields [6].

$$\sigma_i^K = \sigma_i^I \times \omega_K \frac{R_{K_p}}{R_K} \tag{4.20}$$

Where R_{Kp} and R_K are the photon emission rates for a particular peak and the total K-shell respectively.

$$\sigma_{Ltotal}^X = \omega_L \times \sigma_{Ltotal}^I \tag{4.21}$$

The comparisons between experiment and theory for carbon induced X-ray production cross sections are given by the following figures (4.12), (4.13) and (4.14):

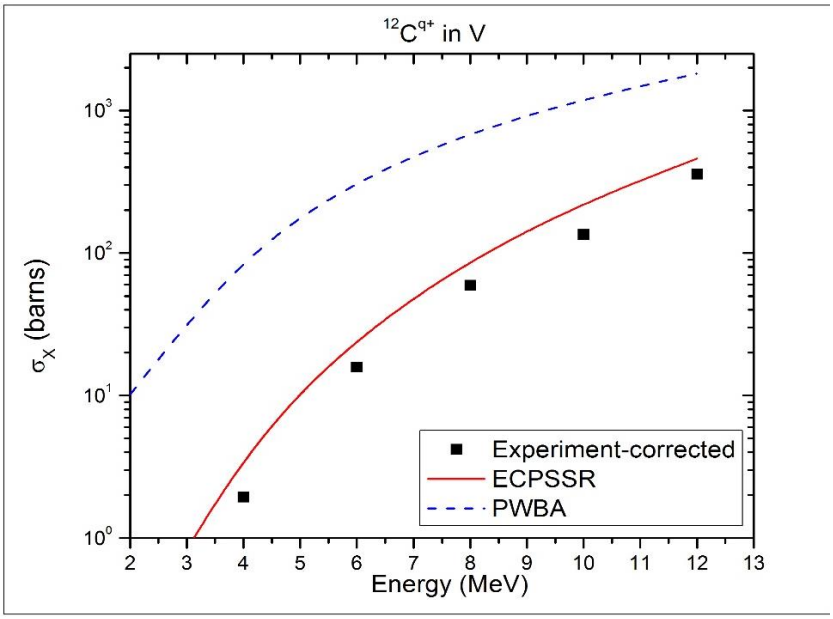

Figure 4.12. *Experimental Carbon induced X-ray production cross sections in V against the PWBA and the ECPSSR theory. (Corrected)*

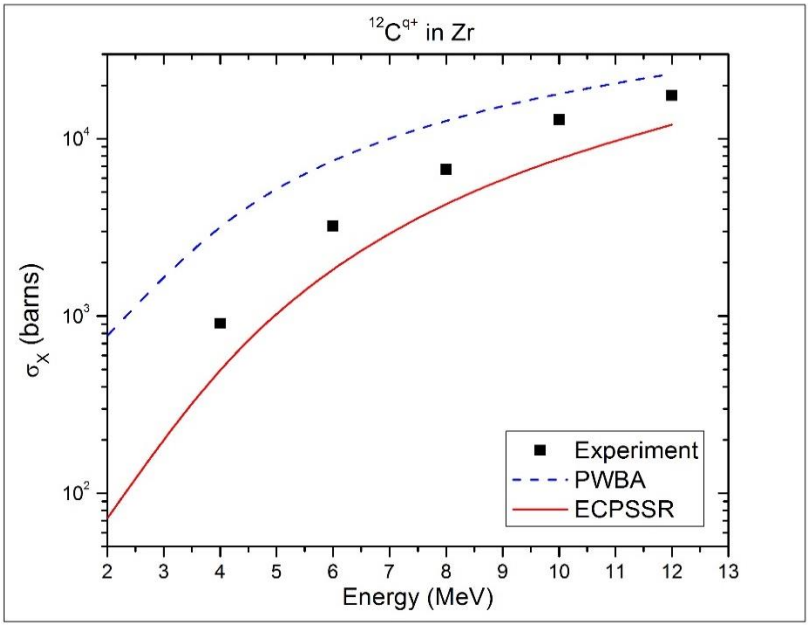

Figure 4.13. *Experimental Carbon induced X-ray production cross sections in Zr against the PWBA and the ECPSSR theory. (Corrected)*

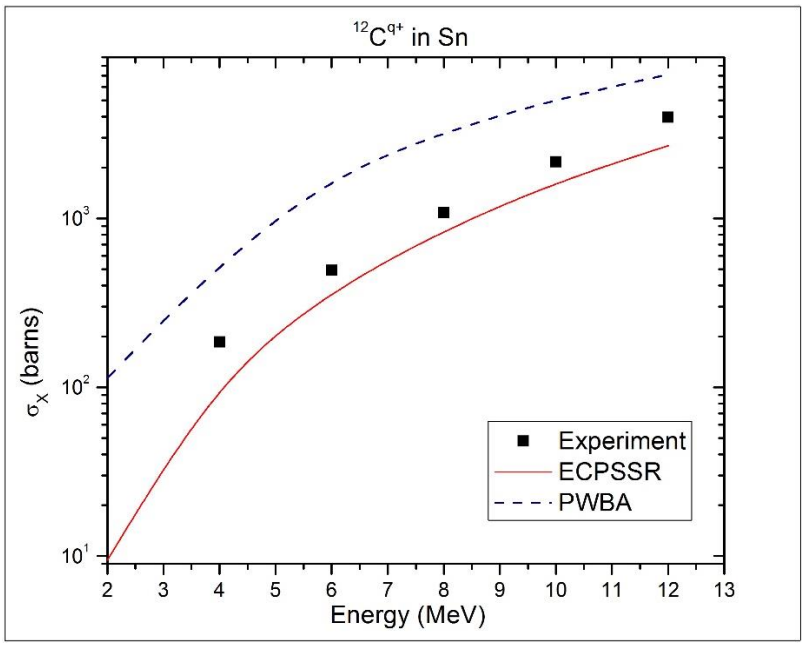

Figure 4.14. *Experimental Carbon induced X-ray production cross sections in Sn against the PWBA and the ECPSSR theory. (Corrected)*

4.5.2. Chlorine-ions energy loss corrections

Table (4.23) describes energy loss for carbon ion beams at 4-12 MeV due to V, Zr and Sn metal oxide films:

$^{35}Cl^{q+}$ Exit Energies

Table 4.23 *7 – 35 MeV Chlorine ion exit energies in Zirconium and Tin.*

Energy (MeV)	**Zr**	**Sn**
7.00	6.21	6.34
14.00	12.96	13.13
21.00	19.89	20.05
28.00	26.89	27.02
35.00	33.90	34.00

Table (4.24) describes energy loss percentages of 7-35 Cl ion beams due to collisions with Zr and Sn metal oxide thin films.

Table 4.24 *Chlorine ion energy loss percentages in Zr and Sn.*

Energy (MeV)	Zr	Sn
7.0	11.3%	9.4%
14.0	7.4%	6.2%
21.0	5.3%	4.5%
28.0	4.0%	3.5%
35.0	3.1%	2.8%

Figure 4.15 describes the loss of chlorine ion beam energy (%) in Zr and Sn due to target stopping powers:

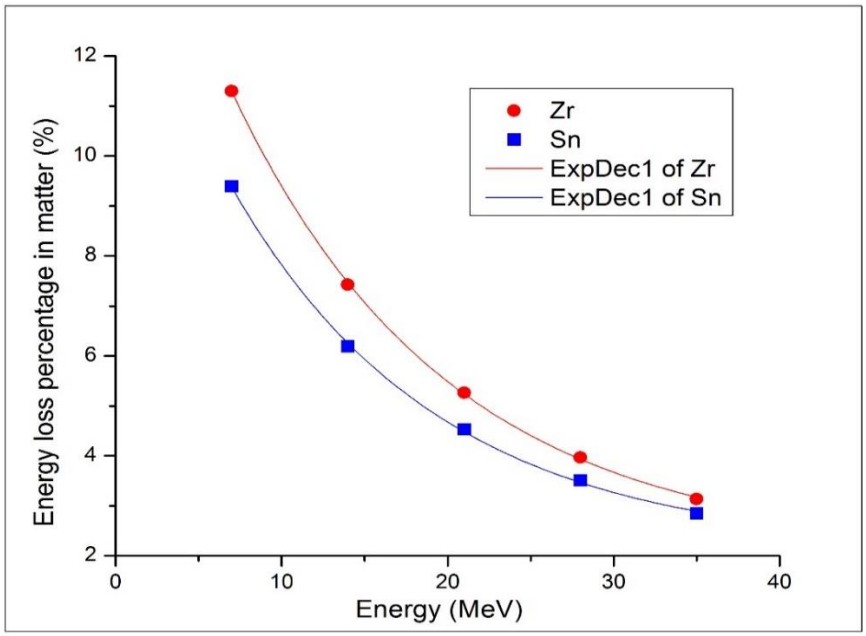

Figure 4.15. *Chlorine ion beam energy loss percentage in Zr and Sn.*

Theoretical cross sections implemented for all carbon-atom combinations are from the ECPSSR theory, obtained using the ERCS08 code [28]. This is because of the observed low discrepancy between the theory and experiment for carbon induced ionization and consequent X-ray production cross sections observed in figures (4.12), (4.13) and (4.14). A high discrepancy between the ECPSSR theory and experiment for chlorine-atom interactions was observed. The PWBA in this case agrees fairly well with experiment. Theoretical cross sections implemented for all chlorine-atom combinations are therefore from the PWBA, obtained using the ERCS08 code [28]. Table (4.25) describes energy loss correction factors for Zr and Sn due to 7-35MeV $^{35}Cl^{q+}$ ion beams:

Cl^{q+} Energy loss correction factors:

Table 4.25 *Chlorine induced X-ray production cross sectional energy loss correction factors in Zirconium and Tin.*

Energy (MeV)	Zr	Sn
7.00	0.91	0.89
14.00	0.94	0.94
21.00	0.96	0.95
28.00	0.97	0.97
35.00	0.97	0.98

The corrected X-ray production cross sections for 7 – 35 MeV $^{35}Cl^{q+}$ in Zr and Sn are described by the following tables:

$^{35}Cl^{q+}$ in Zr

Table 4.26 *Experimental X-ray production cross sections in Zr due to 7 – 35 MeV Chlorine ion beams. (Corrected)*

Energy (MeV)	σ_X(raw) (b)	σ_X(corrected) (b)	PWBA (b)	ECPSSR (b)
7.00	13296.10	12043.52	9522.32	19.66
14.00	30354.56	28836.65	41510.40	651.12
21.00	39773.38	38568.78	87334.63	4575.03
28.00	59243.15	58174.37	137686.01	15110.24
35.00	71085.80	70121.56	186858.90	34246.31

$^{35}Cl^{q+}$ in Sn

Table 4.27 *Experimental X-ray production cross sections in Sn due to 4-12 MeV Chlorine ion beams. (Corrected)*

Energy (MeV)	σ_X(raw) (b)	σ_X(corrected) (b)	PWBA (b)	ECPSSR (b)
7.00	3678.99	3291.90	1531.51	4.69
14.00	11516.89	10894.39	8675.68	94.74
21.00	18229.16	17459.43	21070.26	552.35
28.00	24961.73	24279.23	37740.93	1926.45
35.00	33154.71	32498.79	57366.44	4759.12

The comparisons between experiment and theory for chlorine induced X-ray production cross sections are given by the following figures (4.16) and (4.17):

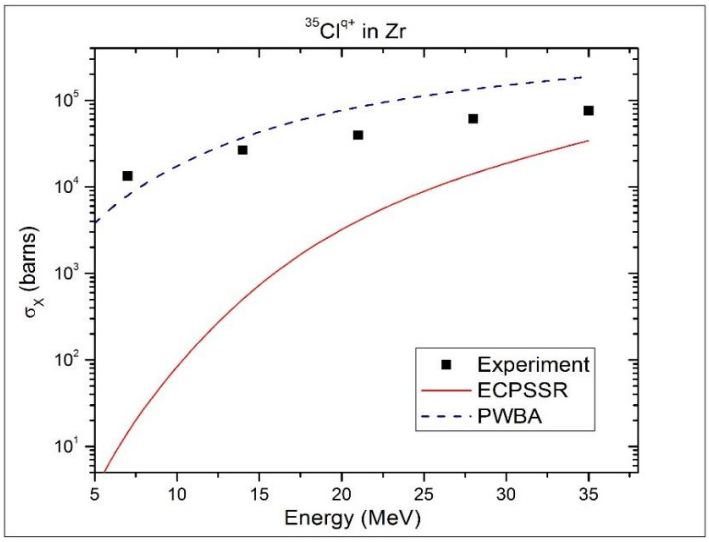

Figure 4.16. *Experimental Chlorine induced X-ray production cross sections in Zr against the PWBA and the ECPSSR theory.*

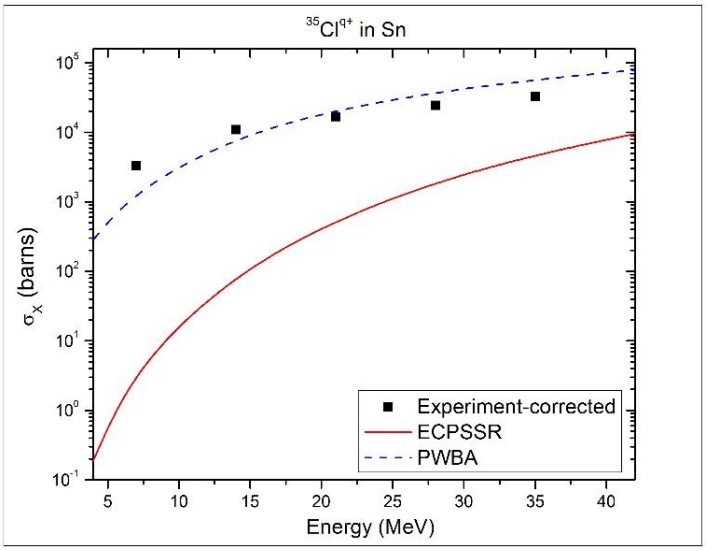

Figure 4.17. *Experimental Chlorine induced X-ray production cross sections in Sn against the PWBA and the ECPSSR theory.*

4.6. Discussion

K-shell X-ray production cross sections

K-shell X-ray production cross sections in Vanadium induced by carbon ion beams were successfully measured and presented in figure (4.15). The ECPSSR theory was seen to agree fairly well with experimental data although slight overestimation of experimental data was observed. The discrepancy between theory and experiment is seen to decrease as the ion energy increases, as shown in figure 4.18.

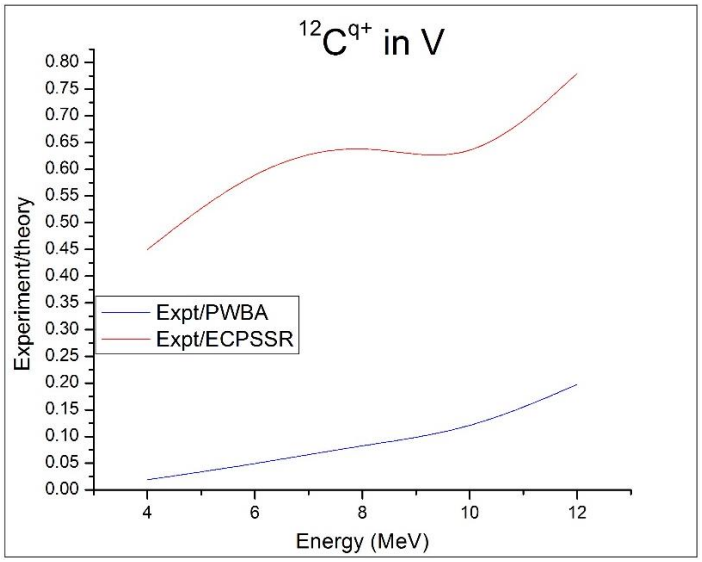

Figure 4.18. *Carbon in vanadium experiment/theory ratios.*

While the ECPSSR theory works for this particular collision system, the PWBA was seen to overestimate experimental data by over an order of magnitude throughout the whole energy range studied, rendering the theory unreliable. The agreement by the ECPSSR theory is due to the relatively low projectile ion mass such that the ratio Z_1/Z_2 categorizes the carbon-vanadium collision as asymmetric [11].

Experimental data for K-shell X-ray production cross sections in vanadium due to carbon ion beams were not found in literature for comparison with data presented in this dissertation.

However, comparisons of experimental cross sections to the PWBA and ECPSSR theories in similar carbon - vanadium (Z_1/Z_2) collision system by Msimanga and co-workers detail similar trends for K-shell cross sections in Titanium due to carbon ion beams [21]. In their work, the Experiment/theory ratio for ECPSSR predictions and experimental data ranges from 0.49 at 6 MeV to 0.9 at 12 MeV.

L-shell X-ray production cross sections

The magnitude of discrepancy was seen to decrease as the energy of the incident ion beam increased for both theories; and the ECPSSR theory became fairly reliable at higher ion beam energies. Observed L-shell X-ray yields in both Zr and Sn due to carbon ions suggest an evident increase in MI and electron capture effects as the target mass increases [21]. This is attested to by relatively higher L-shell X-ray energy shifts for Zr and Sn respectively. While the X-ray production cross section in zirconium and tin significantly increase due to these effects, the ECPSSR theory, although following the same trend, was seen to underestimate data for both zirconium and tin targets. The discrepancy between experiment and the ECPSSR theory in the case of Zr due to carbon projectiles is described by the variation in the ratio $\sigma_{Expt}/\ \sigma_{Theory}$ from 1.61 to 1.47. Similarly, for Sn the ratio varies from 1.425 to 1.44. This is shown in figure 4.19 below:

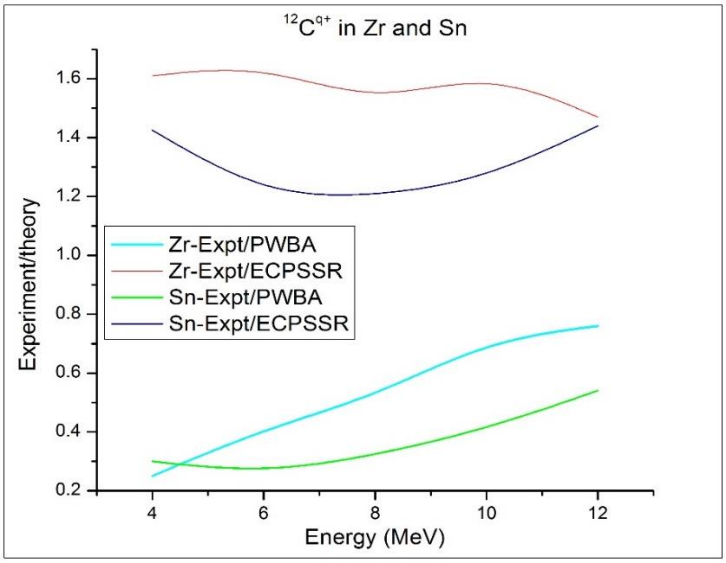

Figure 4.19. *Carbon in zirconium and tin experiment/theory ratios.*

The theory's predictive accuracy of experimental L-shell cross sections in zirconium was seen to range between 62 – 68 %, while higher values for tin based cross sections due to carbon ranged between 89 - 97%. The relatively better predictive accuracy of the ECPSSR theory for C-Sn collisions is due to the large mass difference between the two. The collision that takes place in this instance is similar to that of a binary encounter, where MI effects due to the carbon projectile (which is relatively light) are minute.

Larger discrepancies for chlorine based interactions were observed to be the case between experiment and the ECPSSR theory, especially at lower energies. The predictive accuracy of the ECPSSR theory for Zr ranged between 612.59 - 2.05 ($\sigma_{Experiment}/\sigma_{Theory}$) from low to high energies respectively; as well as 701.90 – 6.83 from low to high energies for Sn cross sections respectively. This is shown in figure 4.20 below;

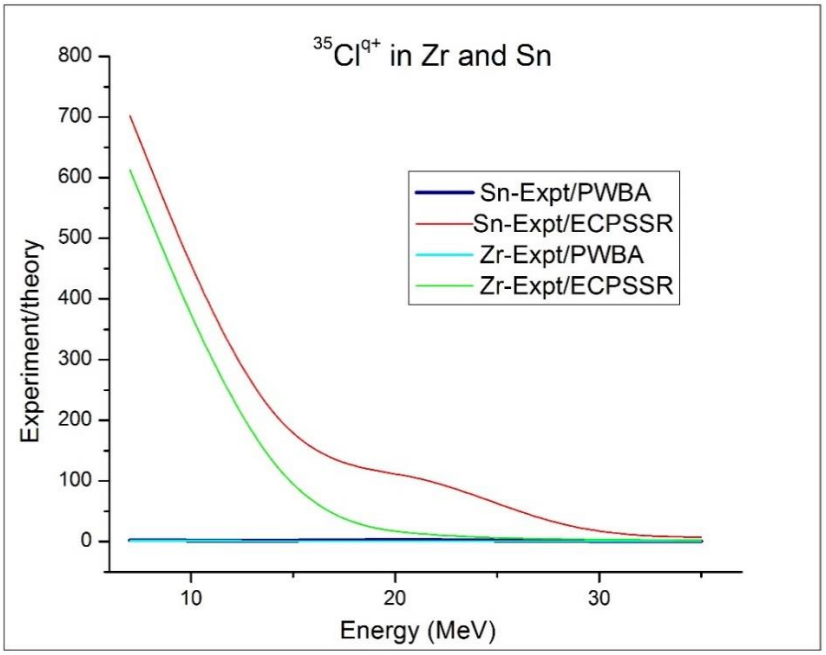

Figure 4.20. *Chlorine in zirconium and tin experiment/theory ratios.*

The poor predictive accuracy by the ECPSSR theory at low ion beam energies suggests that a mechanism unaccounted for by the theory is highly at play. With heavier projectiles, Multiple Ionization can be induced at lower energies [11, 18]. This in effect causes an increase in ionization probabilities which leads to the emission of multiple X-ray photons even at low energies, hence an increased X-ray production cross section.

The PWBA was seen to agree fairly well with chlorine based experimental data. This agreement was seen to be higher for Sn L-shell cross sections due chlorine ion beams. The PWBA, which describes the collision between the ion and projectile as a binary encounter, has not been corrected for any of the mechanisms that take place during a heavy ion-atom collision (i.e. energy loss, electron capture or electronic system perturbation). A disagreement between the theory and experiment is highly expected, which is not the case for chlorine based interactions. A plausible reason to this is that both experiment and theory seem to agree by coincidence. This coincidental

agreement seems to arise due to the PWBA's typical overestimation which seems to agree with cross sections that have increased due to increase MI effects. The increased agreement between the PWBA and experimental Sn cross sections occurs due to increased MI effects due to chlorine as Sn has a much bigger electron cloud than Zr. The 'reducing' discrepancy by the PWBA as both the projectile mass and target mass increases suggests that the PWBA will most likely underestimate experimental data just as the ECPSSR theory for higher than chlorine projectiles. This, according to the mentioned observation, would be the case for targets heavier than Sn, using MeV chlorine ion beams.

Carbon based data was observed to cover a wide cross section power range (e.g. 10^1 - 10^5 barns) while in the case of chlorine beams the experimental cross section range was fixed between at least two to three powers (e.g. $10^3 – 10^5$). The ECPSSR theory was seen to consistently follow a similar trend as that due to lighter ion beams (i.e. wider cross section power range). Higher X-ray production cross sections observed in either Zr or Sn due to Cl compared to carbon ion beams suggested increased X-ray production in the target atoms due to increased MI effects as the target mass increased. This is because of the vast number of electronic interactions that take play during encounters with larger projectile masses.

Large discrepancies between theory and experiment in chlorine-target atom collisions suggest that minor changes were effected by the ECPSSR theory's inherent corrections for deviations where the charge of the projectile is not a point charge and is slower than target electrons. The fair agreement between the ECPSSR theory and carbon induced cross sections compared to the PWBA indicated that the ECPSSR's corrections were successfully effected. This is because of the relatively low mass of carbon compared to chlorine. The ECPSSR theory is seen not to account

for heavy ion-atom interactions. This is because the theory is designed to correct for changes where the projectile ion remains a light ion and thus the encounter between the projectile and the target atom is considered a binary encounter [10]. On the contrary, interactions due to heavier ions are quasi-molecular, where the ionization of the target atom is not only due to direct ionization nor electron capture alone, but also through the interaction of the electron clouds of both the projectile and target. This then leads to increased ionizations of both the projectile and target atom, hence an increased X-ray production cross section. It is because of the ECPSSR theory's foundation on the binary encounter instead of the quasi-molecular encounter [9, 10], that the inherent corrections of the theory do not account for effects such as Multiple Ionization [9], which has been seen to greatly affect the extent to which X-ray are produced from a target atom, and thus the X-ray production cross section.

Chapter 5
Summary and Conclusion

The implementation of heavy ion PIXE depends on a rich database of reliable physical parameters such as ionization and X-ray production cross sections. Publicly available theoretical ionization cross section codes based on the PWBA and ECPSSR theories have been known to be fairly accurate for proton cross section predictions. While this is the case, it has unfortunately not been the case for heavy ion-atom interactions. The principal aim therefore, of the work presented in this dissertation, was to contribute towards the improvement of Heavy Ion PIXE through the measurement and provision of MeV carbon and chlorine induced X-ray production cross sections in metal oxide targets. This data can be used for the improvement and/or development of new empirical codes for the approximation of ionization and X-ray production cross sections.

Data presented in this work has shown that both the PWBA and ECPSSR theory based cross sections cannot simply be extrapolated for heavy ion induced interactions. While carbon based interactions show a fair agreement between experiment and theory; the increasing discrepancy as the mass of the projectile increases attests to the suggestion that the preferred ECPSSR theory cannot be relied upon for heavier projectiles either. It has been shown in chapter 4 that the inherent corrections of the ECPSSR theory work well for relatively light projectiles, as seen in the case of carbon based interactions. These corrections however bear little effect for heavy ion based collisions.

Results have indicated that heavy ion induced collisions are subject to MI effects. The extent of MI has been seen to increase with increasing projectile and target mass for heavy ion based

interactions. This has suggested that the type of interaction that takes place during heavy ion-atom collisions is within the context of a quasi-molecule, due to the high electronic interaction between the projectile and the target atom. As both the PWBA and ECPSSR theory are based on the binary encounter; they do not describe heavy ion based interactions well.

These findings suggest modifications to existing theories such as the ECPSSR theory by incorporating mechanisms induced by heavy ion projectiles, such as MI and also special Coster-Kronig and Auger transitions. In addition to this, a modification to existing heavy ion induced fluorescence yields used for the conversion of ionization to X-ray production cross sections is needed. This indicates that much more work is needed to be done in terms of experimental X-ray production and ionization cross sections, along with fluorescence yields. A suggested theory that would better describe heavy ion based interactions is the Molecular Orbital Theory (MOT) [7, 11, 21, 40], as it describes the heavy projectile-target collision as a quasi-molecule. A new model based on this theory would be best suited for heavy ion cross section predictions.

However, for the implementation of both classical PIXE and HI-PIXE, an improvement to an existing theoretical model with sufficient experimental support and an inherent integration of both the binary encounter and MOT would be a better suitable model.

Future work in this project should aim to extend the range of projectile and target masses, and to compare heavy ion induced X-ray production cross sections to formulations based on MOT theory calculations.

Appendix A: Physical parameters

Table A1. *Table of target element physical parameters*

Element	**Z**	**A *(g/mol)***	$\boldsymbol{\rho_{Atm}}$ $(\boldsymbol{atoms/cm^3})$	$\boldsymbol{\rho_m(g/cm^3)}$
V	23	50.942	6.51×10^{22}	3.240
Zr	40	91.224	4.49×10^{22}	3.604
Sn	50	118.710	3.90×10^{22}	4.300

Constants:

$N_A = 6.023 \times 10^{23}{}_{\text{atoms}}$

$\Delta\Omega = 0.04617\ sr$

Appendix B: Tables of inverse-stopping powers against respective variable energies for the determination of ion exit energies

4-12 MeV Carbon induced in Vanadium:

Table B1. *Y(E) values for Carbon in Vanadium exit energy determinations.*

E	**4MeV V**	**E**	**8MeV V**	**E**	**12 MeV V**
5	-0.00065	9	-0.0053519	13	-0.006069
4	2.16E-05	8	1.91E-05	12	-1.78E-05
3	-0.00499	7	0.0049939	11	0.0060031
2	-0.02625	6	0.0093104	10	0.0117712
1	-0.11155	5	0.0124498	9	0.017438
E	6MeV V	E	10 MeV V		
8	-0.00931	11	-0.0057405		
7	-0.00433	10	2.761E-05		
6	-1.7E-05	9	0.0056944		
5	0.003123	8	0.0110654		
4	0.003796	7	0.0160402		
3	-0.00121	6	0.0203567		

4-12 MeV Carbon induced in Zirconium:

Table B2. *Y(E) values for Carbon in Zirconium exit energy determinations.*

E	**4MeV Zr**	**E**	**8MeV Zr**	**E**	**12MeV Zr**
5	0.000588	9	-0.009193	13	-0.009001
4	-5E-06	8	-4.56E-05	12	3.2035E-05
3	-0.01141	7	0.0084223	11	0.00922684
2	-0.04833	6	0.0155572	10	0.01863843
1	-0.16975	5	0.0200265	9	0.02798246
E	6MeV Zr	E	10MeV Zr		
8	-0.01563	11	-0.009436		
7	-0.00716	10	-2.42E-05		
6	-2.3E-05	9	0.0093198		
5	0.004446	8	0.0184671		
4	0.003853	7	0.0269351		
3	-0.00755	6	0.03407		

4-12 MeV Carbon induced in Tin:

Table B3. *Y(E) values for Carbon in Tin exit energy determinations.*

E	4MeV Sn	E	8MeV Sn	E	12MeV Sn
5	0.005032	9	-0.0046351	13	-0.006742
4	-2.98E-06	8	2.781E-06	12	-1.92E-05
3	-0.014898	7	0.0036595	11	0.0063319
2	-0.056624	6	0.0058081	10	0.0123371
1	-0.209498	5	0.0054841	9	0.0177109
E	6MeV Sn	E	10MeV Sn		
8	-0.005795	11	-0.0059491		
7	-0.002139	10	5.606E-05		
6	1.01E-05	9	0.0054299		
5	-0.000314	8	0.0100678		
4	-0.005349	7	0.0137245		
3	-0.020244	6	0.0158731		

7 – 35 MeV Chlorine induced in Zirconium:

Table B4. *Y(E) values for Chlorine in Zirconium exit energy determinations.*

E	7MeV Zr	E	21MeV Zr	E	35MeV Zr
8	0.0085339	23	0.00038454	36	-0.0001653
7	-2.66E-06	20	-0.0003807	35	-8.797E-07
6	-0.011372	18	-0.0014868	33	0.00040872
5	-0.026835	17	-0.0022978	30	0.00065935
4	-0.048449	16	-0.0032919	28	0.00091076
E	14MeV Zr	E	28MeV Zr		
15	0.001581	30	8.074E-05		
14	7.279E-07	28	9.981E-05		
13	-0.001913	25	-0.0001909		
12	-0.004394	23	-0.0009561		
11	-0.007503	20	-0.0020622		

7 – 35 MeV Chlorine induced in Tin:

Table B5. *Y(E) values for Chlorine in Tin exit energy determinations.*

E	7MeV Sn	E	21MeV Sn	E	35MeV Sn
8	0.01033277	23	0.001286715	36	0.00012565
7	5.387E-06	20	-0.001310932	35	2.4194E-06

6	-0.0135281	18	-0.004075729	33	-0.0004898
5	-0.0319999	17	-0.005756232	30	-0.0012148
4	-0.058472	16	-0.007693171	28	-0.0022377
E	14MeV Sn	E	28MeV Sn		
15	0.00260234	30	-0.000212692		
14	2.1906E-06	28	-0.001619161		
13	-0.0030563	25	-0.003521285		
12	-0.0066667	23	-0.006118932		
11	-0.0109822	20	-0.008883729		

Appendix C: Tables for the determination of energy loss corrections factors

Stopping powers at initial ion energies:

Table C1. *S(E) values for carbon in V, Zr and Sn at initial ion energies.*

S(E)	(keV/micron)		
Carbon	V	Zr	Sn
4	1591.445	1426.227	1315.333
6	1553.462	1398.322	1317.409
8	1483.934	1325.833	1283.906
10	1411.602	1251.522	1240.586
12	1343.372	1184.307	1195.364

Table C2. *S(E) values for chlorine in Zr and Sn at initial ion energies.*

Chlorine	Zr	Sn
7	3380.71	3131.02
14	4442.78	4127.7
21	4722.885	4530.605
28	4750.03	4680.63
35	4694.859	4740.37

Ion exit energies:

Table C3. *S(E) Carbon and Chlorine ion exit energies.*

	Exit Energy		
Carbon	V	Zr	Sn
4	3.71078909	3.666525308	3.733842367
6	5.71769168	5.673049943	5.733422289
8	7.7303269	7.689999031	7.740201621
10	9.74347169	9.707374132	9.748967423
12	11.755871	11.72309007	11.75811809
Chlorine	V	Zr	Sn
7	0	6.209535911	6.366438103
14	0	12.96120695	13.16475991

21	0	19.89571392	20.08323208
28	0	26.88936699	27.05287452
35	0	33.90226685	34.04078613

Stopping powers at ion exit energies:

Table C4. *S(E) values for carbon and chlorine in V, Zr and Sn at ion exit energies.*

Stopping powers at exit energies		
V	Zr	Sn
1591.314	1438.45	1310.072
1563.694	1394.378	1320.087
1496.391	1338.42	1289.396
1422.652	1271.94	1246.259
1353.277	1191.474	1201.065
V	Zr	Sn
0	3175.728	3003.565
0	4352.476	4030.847
0	4707.846	4510.836
0	4761.529	4661.239
0	4738.047	4725.054

(Ef+Ei)/2 ion energies:

Table C5. *Carbon and Chlorine (Ef+Ei/2) energies.*

Ei+Ef/2		
V	Zr	Sn
3.855394544	3.833263	3.866921184
5.85884584	5.836525	5.866711144
7.86516345	7.845	7.87010081
9.871735843	9.853687	9.874483711
11.87793551	11.86155	11.87905905
V	Zr	Sn
0	6.604768	6.683219052
0	13.4806	13.58237995
0	20.44786	20.54161604
0	27.44468	27.52643726
0	34.45113	34.52039307

Stopping powers at (Ef+Ei/2) ion energies:

Table C6. *S(E) values for carbon and chlorine in V, Zr and Sn at (Ef+Ei/2) energies.*

Stopping powers at Ei+Ef/2			
	V	Zr	Sn
4	1591.724	1435.226	1312.921
6	1558.677	1390.275	1318.858
8	1490.085	1333.632	1286.678
10	1416.906	1265.392	1243.38
12	1347.939	1185.595	1198.093
7	0	3280.947	3069.464
14	0	4400.204	4075.228
21	0	4718.02	4528.951
28	0	4761.897	4665.663
35	0	4731.642	4732.862

The energy loss correction factor (broken into sections):

$$F = \underbrace{\frac{1}{\Delta x \times \sigma_i}}_{\mathbf{A}} \times \left[\underbrace{\frac{E_i - E_f}{6}}_{\mathbf{B}} \times \left[\frac{\sigma_i(Ei)}{S(E)_{Ei}} + \underbrace{\frac{\sigma_i(Ef)}{S(E)_{Ef}}}_{\mathbf{C}} + 4 \left[\frac{\sigma_i\left(Ef + Ei/2\right)}{S(E)_{\left(Ef+Ei/2\right)}} \right] \right] \right]$$

Table 'A' values of the energy loss correction factor:

Table C7. *A values for the determination of energy loss correction factors.*

	V	Zr	Sn
A (1/distance x theor.cross sections)			
4	1.28238504	0.0075564	0.042624912
6	0.21084812	0.0021862	0.013219732
8	0.0610057	0.0009611	0.005773892
10	0.02432849	0.0005419	0.003015377

12	0.01196268	0.0003566	0.001831756
7	0	0.0004491	0.003226836
14	0	0.000103	0.000569631
21	0	4.897E-05	0.000234545
28	0	3.106E-05	0.000130944
35	0	2.289E-05	8.61467E-05

Table 'B' values of the energy loss correction factor:

Table C8. *B values for the determination of energy loss correction factors.*

	V	Zr	Sn
B (Ei-Ef)/6			
4	48.20181878	55.57911537	44.35960543
6	47.05138651	54.49167613	44.42961853
8	44.94551665	51.66682812	43.29972985
10	42.75471901	48.77097799	41.83876285
12	40.68816308	46.15165425	40.3136509
7		131.7440149	105.5936495
14		173.1321747	139.2066825
21		184.0476799	152.7946536
28		185.1055024	157.8542468
35		182.9555253	159.8689783

Table 'C' values of the energy loss correction factor:

Table C9. *C values for the determination of energy loss correction factors.*

	V	Zr	Sn
C (measured XP-CS on S(E))			
4	0.012386	2.103402	0.468392
6	0.08831	7.762175	1.594327
8	0.331724	18.99869	3.798119
10	0.897197	36.14622	7.618906
12	1.949209	59.16243	13.14662
7	0	15.32954	2.616162

14	0	52.54252	11.88438
21	0	106.1477	26.62506
28	0	168.4905	46.87941
35	0	232.4064	70.9057

Energy loss correction factor $= A \times B \times C$

Table of energy loss correction factors:

Table C10. *Energy loss correction factors for carbon and chlorine ion beams in V, Zr and Sn.*

	Energy loss correction factors F		
	V	Zr	Sn
4	0.76562934	0.88338664	0.885646434
6	0.876094782	0.92470645	0.936424246
8	0.909565437	0.94341595	0.949560088
10	0.933225772	0.95526881	0.961198633
12	0.948756995	0.97363071	0.970809169
7	0	0.90707472	0.891413964
14	0	0.9372545	0.942388162
21	0	0.95670969	0.954169894
28	0	0.96879234	0.968997428
35	0	0.97320788	0.976526897

References:

1. A.E. Johansson, T.B. Johansson, Analytical application of particle induced X-ray emission, Nucl. Instr. Meth 137(1976) 473-516.
2. J. Reyes-Herrera, J. Miranda, K X-ray emission induced by 12c4+ and 16O5+ ion impact on selected lanthanoids, Nucl. Instr. Meth. B 267(2009) 1767 – 1771.
3. M. Msimanga et al., K-shell X-ray production cross sections in Ti by 0.3-1.0MeV/u 12C and 28Si for heavy ion PIXE, Nucl. Instr. Meth. B 380(2016) 90-93.
4. I. Medeiros et al., Brazilian J.Phys, vol. 35, no. 3B, September 2001.
5. S. Nagashima et al., Nucl. Instr. Meth B 109/110 (1996) 658-661.
6. D. Cohen et al., Nucl. Instr. Meth B 109/110(1996) 218-226.
7. I. Bogdanovic et al., L-shell ionization of Cd, Sb, Te, Ba, La, Eu, Tb and Yb by 16O ions in the energy range from 0.19 to 0.75 MeV u-1, Nucl. Instr. Meth. B 150(1999) 18-26.
8. M. Pajek et al., K-shell ionization by low-energy 14N ions, Nucl. Instr. Meth.B 152(1999) 27-35.
9. M. Batic et al., ISICSoo: a class for the calculation of ionization cross sections from ECPSSR and PWBA theory. Instituto Nazionale di fisica nucleare, sezione di Genova, Via dodecaneso 33, 16146 genova, Italy.
10. W. Brandt, G. Lapicki, Phys. Rev. A 20 (1979 465.
11. J. Miranda et al., X-ray production induced by heavy ion impact: challenges and possible uses, Revisita Mexicana de fisica 53(2007)29-32.
12. GW Grime, High-Energy Ion beam anaylsis. University of surrey, Guildford, UK. Elsevier, 2014.

13. J.W. Mayer and E. Rimini. *Ion Handbook for Material Analysis*. Academic Press, New York, San Francisco, London, 1977.
14. M. Mayer, SIMNRA User's Guide, Report IPP/113, Max-Planck-Institut fur Plasmaphysik, Garching, Germany, 1997.
15. I. Gorlachev et al., X-ray production cross section for K-, L- and M-shell by 14 MeV and 19.6 MeV nitrogen, Nucl. Instr. Meth.B 330(2014) 86-90.
16. J.E. Ziegler et al., The Stopping and Range of Ions in Solids, Vol. 1 of The Stopping and Ranges of Ions in Matter. Pergamon Press, New York, 1985.
17. E. Cengiz et al., K-shell X-ray fluorescence parameters of some heavy elements and compounds, Rad. Phys. Chem 80(2011) 328-334.
18. F. Richtmyer, The Multiple Ionization of Inner Electron Shells of Atoms, Cornell University, Ithaca, New York, 1936.
19. J.A. Tanis et al., Phys. Rev. A 31 (2) (1985) 750.
20. J. Campbell. Atomic data and Nuclear Data Tables 85 (2003) 291-315
21. M. Msimanga *et al.*, Nucl. Instr. Meth B 440(2019) 186-190.
22. J.D. Cutnell, K.W. Johnson, Introduction to Physics, John Wiley & Sons, Inc, USA, 2008.
23. I. Orlic et al., Nucl.Instr. Meth B 363(2015) 37 - 41.
24. M Kiisk et al., Nucl. Instr. Meth B 172(2000) 182-187.
25. S. Johansson et al., Particle-induced X-ray Emission Spectroscopy (PIXE), Wiley-Interscience, 1995.
26. D. Cohen et al., Nucl. Instr. Meth B 363 (2015) 7-18.

27. A.J. Kreiner, K X-ray production induced by 12C on several elements, Nucl. Instr. Meth. B 201(2003) 317-324.
28. V. Horvat, ERCS08: A FORTRAN program equipped with a Windows graphics user interface that calculates ECPSSR cross sections for the removal of atomic electrons, Comp. Phys. Com 180 (2009) 995-1003.
29. IAEA coordinated research project (CRP) #F11019: "Development of molecular concentration mapping techniques using MeV focused ion beams".
30. I. Medeiros et al., Brazilian J. Phys, vol. 35, no. 3B, September 2001.
31. I. A. E. Agency. Instrumentation for PIXE and RBS. International Atomic Energy Agency, 2000.
32. C. Ryan, PIXE and the nuclear microprobe: Tools for quantitative imaging of complex natural materials, Nucl. Instr. Meth B 269 (2011) 2151-2162.
33. National Electronics Corp, Source of Negative Ion by Cesium Sputtering- SNICS II, 2017.
34. M. Beno et al., A new 6MV Tandem accelerator in TRNAVA, Mat. Sci and Tech, No.1, 2015.
35. J. Pamela, The physics of production, acceleration and neutralization.
36. G. Berg, An introduction to Ion-Optics, JINA, University of Notre Dame, 2005.
37. D. Banas et al., Atomic physics in heavy ion-atom collisions, Darmstadt, Germany.
38. A. Zucchiatti et al., Nucl. Instr. Meth B 407 (2017) 1 - 4.
39. I. Gorlachev et al., X-ray production cross section for K-, L- and M-shell by 14 MeV and 19.6 MeV nitrogen, Nucl. Instr. Meth.B 330(2014) 86-90.
40. C. Ciortea et al., K-shell ionization in (0.2-1.75) MeV/u Fe, Co + Cr and Fe + Cu collisions, Nucl. Instr. Meth. B 235(2005) 342-346.

41. R Mehta, L-shell x-ray production by 2-12MeV carbon ions in fifteen selected elements from copper to lead, J.phys. Mol. Opt. Phys. 28(1995) 1187-1200.
42. A.P.L. Bertol et al., L-shell X-ray production cross sections induced by protons and alpha-particles in the 0.7-2.0 MeV/amu range for Ru and Ag, Nucl. Instr. Meth. B 318(2014) 19-22.
43. I. Bogdanovic, S. Fazinic, L-shell X-ray production for Rh, Ag, Cd, Sb and I with protons in the energy range from 1.6 to 5.2 MeV, Mol. Opt. Phys. 29(1996) 2021-2031.
44. A.C. Scafes, K X-ray production and rec cross sections in 0.75-2.5 MeV/u 32S, 35Cl ions on Cu atomic collisions. Romanian Reports in physics, Vol. 66, No. 3, P. 630-648, 2014.
45. J. Miranda, G Lapicki, Experimental cross sections for L-shell X-ray production and ionization by protons, Atomic data and Nuclear data tables 100(2014) 651-780.
46. M. Kiisk et al., Characteristic X-ray production in heavy ion collisions, Nucl. Instr. Meth. B 172(2000) 182-187.
47. M. Nastasi et al., Ion Beam Analysis: Fundamentals and Applications, CRC Press, 2014.
48. Z. Smit, G. Lapicki, Energy loss in the ECPSSR theory and its calculation with exact integration limits, J. Phys. B: At. Mol. Opt. Phys. 47 055203.
49. D. Cohen et al., Nucl. Instr. Meth B 363 (2015) 7-18.
50. F. Hinterberger, Ion optics with electrostatic lenses, University of Bonn, Germany.
51. R. Protz et al., Nucl. Instr. Meth B. 77 (1993) 509-516.
52. P. Nel et al., Nucl. Instr. Meth A 619(2010) 306-310.
53. F. Fernandes et al., Nucl. Instr. Meth B 417(2018) 19-25.
54. T. Calligaro et al., Nucl. Instr. Meth B 363(2015) 135-143.
55. M.J. Ozafran et al., Nucl. Instr. Meth B 201(2003) 317-324.

56. Ansto, Calculated K, L and M –shell X-ray line intensities for light ion impact of selected targets from Z=6 to 100, 2011.
57. C. Brundle et al., Encyclopedia of Materials characterization, Butterworth-Heinemann, Stoneham, USA, 1992. 240, 338